

Article

The Paleoenvironment and Mechanisms of Organic Matter Enrichment of Shale in the Permian Taiyuan and Shanxi Formations in the Southern North China Basin

Yanan Wang^{1,2,3}, Xiulei Cheng⁴, Kai Fan⁵, Zhipeng Huo^{3,6,*} and Lin Wei^{1,2,*}

- ¹ School of Energy Resources, China University of Geosciences, Beijing 100083, China
² Key Laboratory of Strategy Evaluation for Shale Gas of Ministry of Land and Resources, China University of Geosciences, Beijing 100083, China
³ School of Resources and Materials, Northeastern University-Qinhuangdao Campus, Qinhuangdao 066004, China
⁴ No.1 Data Acquisition Branch Company, No.1 Geo-Logging Company, Daqing Drilling & Exploration Engineering Corporation, Daqing 163000, China
⁵ CNOOC EnerTech-Drilling & Production Co., Ltd., Tianjin 300452, China
⁶ National Engineering Research Center of Offshore Oil and Gas Exploration, Beijing 100028, China
* Correspondence: huozhipeng521@163.com (Z.H.); linwei@cugb.edu.cn (L.W.); Tel.: +86-134-8873-0863 (Z.H.); +86-155-1030-9590 (L.W.)

Abstract: The organic-rich shale of the Permian Taiyuan Formation (TYF) and Shanxi Formation (SXF) in the Southern North China Basin (SNCB) is considered a potential shale gas source. The shale was formed in a marine-continental transitional sedimentary environment, which has rarely been studied, with the enrichment mechanisms of organic matter (OM) remaining unclear. This study investigated the controlling factors and enrichment mechanisms of OM by analyzing the total organic carbon (TOC) content, paleoclimate, paleoproductivity, sedimentation rate, redox, and paleosalinity. The TOC of the TYF ranged from 0.92 to 7.43 wt.%, with an average of 2.48 wt.%, which was higher than that of the SXF (TOC = 0.36–5.1 wt.%, average of 1.68 wt.%). These geochemical indices suggest that both the TYF and SXF were deposited in warm and humid paleoclimates, with relatively high biological productivity and sedimentation rates. During the deposition process, the TYF experienced frequent transgression and regression events, leading to an enhancement of water reducibility, a relatively high sedimentation rate, reduced OM oxidation, and rapid deposition of OM, which were conducive to the preservation of OM. Moreover, a high biological productivity increased respiratory oxygen consumption in the water column, which could lead to OM accumulation. However, the regression event experienced by the SXF reduced the paleoproductivity and sedimentation rate and increased water oxidation, leading to a decrease in OM. The main controlling factors for the enrichment of OM in the TYF and SXF were the sedimentation rate, paleoproductivity, and redox conditions, thus establishing the enrichment models for OM in the TYF and SXF. This study is conducive to understanding shale enrichment mechanisms and guiding shale gas exploration.

Keywords: paleoenvironment; organic matter enrichment; enrichment model; shale; marine-continental facies; southern north China basin



Citation: Wang, Y.; Cheng, X.; Fan, K.; Huo, Z.; Wei, L. The Paleoenvironment and Mechanisms of Organic Matter Enrichment of Shale in the Permian Taiyuan and Shanxi Formations in the Southern North China Basin. *J. Mar. Sci. Eng.* **2023**, *11*, 992. <https://doi.org/10.3390/jmse11050992>

Academic Editors: Wenming Ji, Guodong Cui and Mianmo Meng

Received: 4 April 2023

Revised: 27 April 2023

Accepted: 2 May 2023

Published: 7 May 2023



Copyright: © 2023 by the authors. Licensee MDPI, Basel, Switzerland. This article is an open access article distributed under the terms and conditions of the Creative Commons Attribution (CC BY) license (<https://creativecommons.org/licenses/by/4.0/>).

1. Introduction

Organic-rich shale is not only a source rock of high-quality conventional oil and gas reservoirs but also a focus of shale oil and gas exploration. It can record important paleoclimatic and paleoenvironmental information (such as paleotemperature, paleoredox, and paleoproductivity) relating to when it is deposited, thus possessing significant value from a scientific research perspective [1–3]. Furthermore, as noted above, study of organic-rich shale also contributes critical information to oil and gas exploration activities, including both understandings of source rock in conventional petroleum systems [4] and of reservoir

rock in unconventional shale gas and shale oil systems [5], and is critical to the evolving understanding of potentially exploitable gas hydrate resources [6,7]. Currently, significant progress has been made in marine and continental shale gas research; however, there is little research on marine-continental transitional shale gas. Marine-continental transitional facies are widely distributed in China, often with multiple lithologies coexisting and rapid changes in lithofacies, and the source and composition of organic matter are complex [8]. Therefore, compared with marine or terrestrial strata, they have distinct characteristics and are a potentially important area of unconventional oil and gas exploration in China.

The accumulation of organic matter (OM) is a complex physicochemical process [9,10]. Previous studies have shown that owing to the complex geological, oceanographic, and climatic histories, it is impossible for a single factor to explain OM accumulation in a sedimentary environment [11]. The accumulation and preservation of OM are controlled and affected by paleoclimate, paleoproductivity, sedimentation rate, redox, and paleosalinity [12–14]. Generally, elemental geochemistry [2] and organic geochemistry [15] are used to qualitatively reconstruct paleoenvironment [16–18]. Several redox-sensitive elements (such as V, U, and Ni) and their ratios (such as U/Th, V/Cr, Ni/Co, and V/(V + Ni)) have been widely used to explain ancient redox conditions [2,19]. Important geochemical indicators that qualitatively characterize paleoclimate include the chemical index of alteration (CIA) and the C-value [20–22].

Factors controlling OM enrichment in marine environments have been widely studied. From different influence mechanisms, they can be divided into the “productivity model” and the “conservation model” [23,24]. In the productivity model, organic matter input is the main reason for its enrichment. In the preservation model, it is believed that the factors of high salinity and anoxic sedimentary environments are the main conditions for the enrichment of organic matter. Unlike marine shale, marine-continental transitional shale is deposited in a sea-and-land interaction environment, with rapid facies changes on the plane, and complex enrichment mechanism of OM, leading to large differences in OM enrichment factors between marine shale and marine-continental transitional shale.

The SNCB is the largest sedimentary basin in China. The Permian is widely distributed and well developed, and its sedimentary types are diverse and rich in biological fossils [25]. The main strata of shale gas in the SNCB are the TYF and SXF, and the shale kerogen is generally type III [26,27]. There are few studies on Permian shale in the SNCB; the geological conditions are complex, and the sedimentary and tectonic evolution are changeable [25]. Presently, the amount of research on shale gas in this area is low [25], and an OM enrichment model has not been established, restricting the objective evaluation of shale gas resources in the basin [28].

This study measured and analyzed TOC, major elements, trace elements, and rare-earth elements to reconstruct the paleoclimate, paleoproductivity, sedimentation rate, paleoredox, and paleosalinity of the Permian TYF and SXF in the SNCB to reveal the enrichment mechanisms of OM in the SNCB, which provide an important basis for shale exploration in this area.

2. Geological Background

Located south of the North China Block and its southern margin (Figure 1), the SNCB is mainly controlled by the structure of the Qinling–Dabian orogenic belt [29]. From the distribution characteristics of the Mesozoic and Cenozoic in the basin, the SNCB is divided from north to south into five structural units: the Kaifeng Depression, the Taikang Uplift, the Zhoukou Depression, the Bengbu Uplift, and the Xinyang Hefei Depression (Figure 1) [29–31].

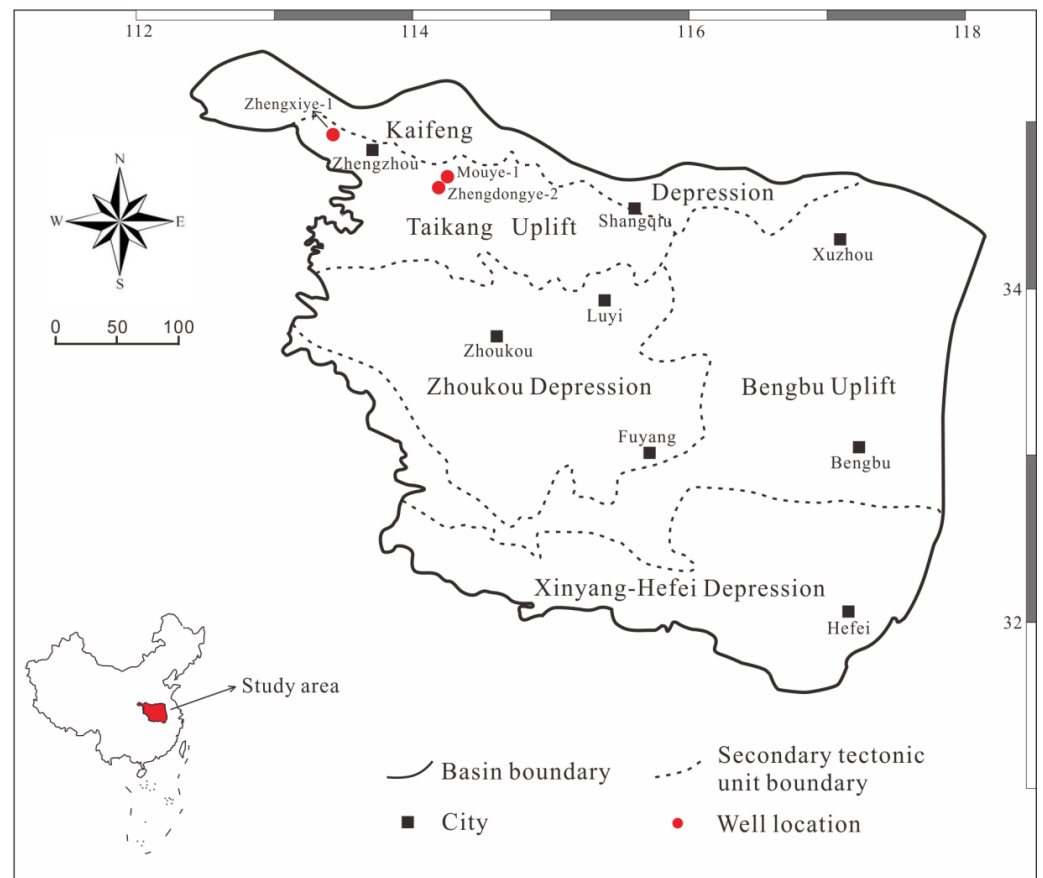


Figure 1. Simplified structural block map of the SNCB with investigated well location.

From the Late Ordovician to the Middle Carboniferous, the SNCB was uplifted due to the Caledonian movement. Owing to long-term weathering and denudation, most parts of the region lack Upper Ordovician, Silurian, Devonian, and lower Carboniferous strata [31,32]. Subsequently, Lower Permian marine-continental transitional strata were immediately deposited on the Upper Ordovician limestone [32]. Controlled by regional tectonic movements, the sedimentation process can be subdivided into three stages. First, Late Carboniferous seawater invaded from the northeast to southwest, forming a unified North China epicontinental sea basin. In this environment, the thickness of the Early Permian sediments is 30–175 m. Second, the collision between the North China and Siberian plates caused large-scale tectonic movement and regression from north to south. The main sedimentary environment in the Permian was a shallow water delta, which transitioned from the epicontinental sea through regression. Finally, the North China plate was uplifted again by compression during the Late Permian, resulting in the complete withdrawal of seawater from the North China platform and the formation of a continental sedimentary environment [26,31–33]. In general, the sedimentary environment of the North China platform from the Early to the Late Permian experienced both marine-continental transitional and lacustrine environments.

The Mouye-1 (MY1) well, drilled in 2014, was the first shale gas exploration well in the SNCB, and shale gas was found in the Upper Paleozoic strata. The Weican-1 well, drilled in the same year, encountered OM-rich shale with a cumulative thickness of 465 m in the Shihezi, TYF, SXF, and Benxi Formations. The Zhengxiye-1 (ZXY1) well, drilled in 2015, also saw good shale gas in the Permian SXF and TYF [34,35]. As of July 2020, the MY1, Zhengdongye-2 (ZDY2), and ZXY1 wells had been drilled northwest of the SNCB to explore for shale gas (Figure 1) [35]. The shale thicknesses in the TYF of the MY1, ZDY2, and ZXY1 wells are 54 m, 31 m, and 12 m, respectively, and the thicknesses of the SXF are 44 m, 14 m, and 16 m, respectively. From the cores, it is apparent that the lithology of

the TYF is mainly grayish black mudstone, dark gray limestone, grayish black sandstone, dark gray sandstone, and dark gray shale, with thin layers of siltstone, coal lines, and barrier coastal facies. The lithology of the SXF is dominated by grayish black mudstone, carbonaceous mudstone, silty mudstone, fine sandstone, and sandstone, which are delta facies (Figure 2).


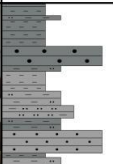

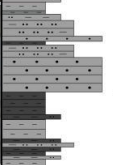

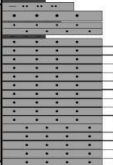

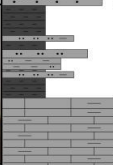






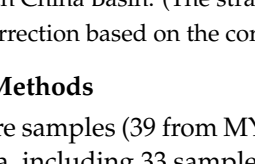
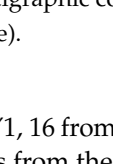
Stratum Formation	Depth (m)	Core images	Lithology	Litology description
Shanxi	2840			Gray black mudstone siltstone interbedding
				Black mudstone and peat deposit, with a set of coal seams developed at the bottom
	2880			Grayish black fine sandstone with brown carbonaceous mudstone and coal line
				Grayish black mudstone with thin layer of siltstone
Taiyuan	2920			Dark gray carbonaceous bioclastic limestone
				Grayish black mudstone with thin layer of siltstone
	2960			Dark gray carbonaceous bioclastic limestone
				Gray black mudstone, intercalated with thin layer of siltstone and coal line in the middle

Figure 2. The stratigraphic column of the Lower Permian Shanxi and Taiyuan Formations (MY1 well) in the Southern North China Basin. (The stratigraphic column data mainly come from core logging and later artificial correction based on the core).

3. Sampling and Methods

Overall, 62 core samples (39 from MY1, 16 from ZDY2, and 7 from ZXY1) were selected from the study area, including 33 samples from the TYF and 29 samples from the SXF. The samples from Well MY1 included both TYF and SXF. The samples from Well ZDY2 were

mainly from the TYF, while those from Well ZXY1 were mainly from the SXF. The lithology is mainly shale with a small amount of coal. The TOC content, major elements (ME), trace elements (TE), and rare-earth elements (REE) of all samples were measured and analyzed.

3.1. TOC Analysis

First, powder with the size of 200 meshes was treated using chemical methods in accordance with the Chinese Standard GB/T19145-2003, and then the sample (100 mg) was treated with 5% HCl for 24 h to remove the inorganic carbon component. Finally, a Leco[®] CS744 analyzer (Equipment source: LECO, St. Joseph, MI, USA) was used to measure the organic carbon content with an accuracy of $\pm 0.5\%$.

3.2. Major Element Analysis

The primary elements (Si, Al, Fe, K, Na, Ca, Mg, Mn, Ti, and P) were tested using the XRF (X-ray fluorescence) method. The XRF tester was a Rigaku ZSX-100e. To mix the organic matter-removed sample (powder) and $\text{Li}_2\text{B}_4\text{O}_7$ evenly, they were poured into a platinum crucible, placed in a high-frequency heating-dissolving machine, and heated to $1150\text{ }^\circ\text{C}$. The melted mixed sample was poured onto a glass sheet and finally placed into an XPF instrument for testing.

3.3. Trace and Rare-Earth Element Analysis

The TE and REE contents were measured using an Agilent 7500a inductively coupled plasma mass spectrometer (ICP-MS), with an analysis error lower than 5%. The sample (powder) with the removed OM was subjected to acid dissolution ($\text{HF}/\text{HNO}_3/\text{HClO}_4 = 2:2:1$). The treated samples were then heated in a pressure-tight Teflon bomb at $200\text{ }^\circ\text{C}$ for 48 h, and the resulting liquid was analyzed using inductively coupled plasma mass spectrometry (ICP-MS). The analytical procedures followed the Chinese National Standards GB/T 14506.1~14-2010 (2010) and GB/T 14506.30-2010 (2010).

4. Results

4.1. TOC

The TOC content of the TYF shale was 0.92–7.43 wt.%, with an average of 2.48 wt.% and a median of 2.24 wt.%. The TOC of coal was 54.45–66.55 wt.%, with an average of 60.5 wt.%. Approximately 51.52 wt.% of the samples were >2 wt.%, which indicates a good source rock [4] (Table 1; Figure 3). The TOC of the SXF shale was 0.36–5.1 wt.%, with an average of 1.68 wt.% and a median of 1.73 wt.%, and the TOC of coal was 58.95–61.29 wt.% (average of 60.5 wt.%), of which approximately 35.48 wt.% of the samples were greater than 2 wt.% (Table 1; Figure 3). Overall, the TOC content of the Lower Permian shale in the SNCB is relatively high, with the TOC content of the shale in the TYF being higher than that in the SXF.

Table 1. ME contents (wt%) of the TYF and SXF in the SNCB.

Well	Sample	Depth (m)	TOC (wt.%)	MEs (wt.%)									
				SiO_2	Al_2O_3	TFe_2O_3	MgO	CaO	Na_2O	K_2O	TiO_2	P_2O_5	MnO
MY1	JX2	2804.81	4.19	41.52	33.71	0.73	0.22	0.10	1.27	2.43	1.15	0.09	0.22
MY1	JX3	2807.74	1	55.00	30.00	1.44	0.36	0.17	1.56	4.55	1.02	0.14	0.36
MY1	JX4	2810.32	0.76	49.12	25.90	6.66	0.73	0.27	1.81	3.85	0.80	0.23	0.74
MY1	JX6	2815.3	0.55	46.92	10.30	22.52	1.46	0.56	1.24	0.72	0.28	0.37	1.46
MY1	JX7	2819.27	0.53	56.31	27.11	2.43	0.50	0.18	1.99	5.40	1.08	0.09	0.50
MY1	JX8	2821.74	1.23	51.32	25.41	3.00	0.90	0.27	3.37	4.99	1.03	0.18	0.89
MY1	JX10	2827.13	1.09	49.31	31.40	2.20	0.40	0.25	2.67	3.93	0.93	0.18	0.40
MY1	JX11	2830.72	0.52	50.81	26.72	2.76	0.76	0.22	4.58	5.66	0.95	0.09	0.76
MY1	JX12	2831.66	0.44	48.82	24.51	3.62	1.03	0.46	3.59	5.35	1.03	0.23	1.05
MY1	JX14	2838.32	0.89	49.12	30.00	0.00	1.04	0.28	3.07	6.53	0.87	0.14	1.05
MY1	JX15	2840.23	0.48	52.61	29.31	2.65	0.53	0.24	3.32	5.61	0.97	0.09	0.53
MY1	JX16	2841.88	2.37	48.63	24.30	3.47	0.85	0.29	2.59	5.08	0.90	0.27	0.85
MY1	JX17	2844.32	2.39	50.92	21.11	4.59	1.08	1.76	3.59	2.99	0.85	0.23	1.08

Table 1. *Cont.*

Well	Sample	Depth (m)	TOC (wt.%)	MEs (wt.%)									
				SiO ₂	Al ₂ O ₃	TFe ₂ O ₃	MgO	CaO	Na ₂ O	K ₂ O	TiO ₂	P ₂ O ₅	MnO
MY1	JX18	2847.16	0.62	56.80	26.30	2.60	0.56	0.22	3.53	5.81	0.75	0.09	0.57
MY1	JX19	2848.82	1.98	48.63	29.91	2.32	0.65	0.32	5.12	4.77	0.70	0.18	0.65
MY1	JX20	2849.51	54.45	2.18	1.79	0.67	0.15	0.21	0.19	0.22	0.03	0.00	0.15
MY1	JX21	2855.01	66.55	0.58	0.55	0.14	0.02	0.07	0.08	0.02	0.02	0.00	0.03
MY1	JX22	2852.36	2.21	42.72	25.72	0.44	0.32	0.06	1.46	10.65	0.92	0.09	0.32
MY1	JX24	2857.02	4.24	41.03	24.81	4.16	0.76	0.17	1.08	11.18	0.82	0.18	0.76
MY1	JX31	2884.3	5.1	44.73	22.71	5.52	1.16	0.43	1.29	9.08	0.88	0.55	1.16
MY1	JX32	2886.27	1.97	44.73	22.71	5.52	1.16	0.43	1.29	9.08	0.88	0.55	1.16
MY1	JX33	2889.34	2.56	45.03	23.11	4.27	1.01	0.13	1.70	8.50	0.73	0.14	1.01
MY1	JX34	2894.31	1.78	47.13	21.90	0.01	1.23	0.85	1.35	8.60	0.72	0.37	1.24
MY1	JX36	2913.2	3.74	43.54	21.41	4.73	1.16	0.34	1.62	5.11	0.77	0.32	1.16
MY1	JX37	2917.42	0.92	47.43	24.01	3.60	1.01	0.22	1.54	6.02	0.83	0.27	1.02
MY1	JX39	2923	1.87	48.52	21.31	0.01	1.08	0.70	1.99	6.05	0.75	0.23	1.08
MY1	JX40	2925.92	1.93	48.52	21.31	3.79	1.08	0.70	1.99	6.05	0.75	0.23	1.08
MY1	JX42	2931.5	1.75	43.54	20.61	1.56	0.65	0.15	1.78	4.10	0.55	0.09	0.65
MY1	JX43	2933.86	4.14	42.42	22.60	5.45	0.76	0.50	1.48	3.93	0.77	0.37	0.76
MY1	JX44	2935.4	61.29	54.21	28.61	0.97	0.60	0.29	1.51	4.89	1.12	0.09	0.61
MY1	JX45	2939.27	1.69	44.52	21.71	4.62	1.08	0.46	1.81	4.58	0.88	0.32	1.08
MY1	JX46	2941.28	2.25	48.63	24.30	4.39	1.08	0.39	1.78	5.13	0.92	0.27	1.08
MY1	JX47	2943.35	0.66	0.34	0.19	0.97	0.00	0.10	0.00	0.02	0.02	0.05	0.00
MY1	JX49	2948.32	58.95	38.53	19.50	4.60	0.70	0.57	1.21	4.41	0.50	0.73	0.70
MY1	JX50	2950.09	5.06	42.94	18.80	5.56	1.08	0.99	1.48	4.00	0.67	0.23	1.08
MY1	JX51	2953.09	1.67	44.73	21.01	5.20	1.13	1.02	2.21	4.07	0.72	0.41	1.14
MY1	JX52	2955.71	1.88	48.22	22.01	4.72	1.48	4.49	2.21	4.99	0.70	0.27	1.48
MY1	JX53	2958.16	2.55	53.31	20.20	0.10	1.06	2.27	2.05	5.40	0.67	0.37	1.06
MY1	JX54	2960.13	1.89	37.74	16.61	2.96	1.13	15.68	1.59	3.93	0.58	0.23	1.14
ZDY2	ZY2-SX-2	2841.67	2.58	56.82	18.48	6.51	1.53	1.02	1.75	4.65	0.93	0.50	0.14
ZDY2	ZY2-TY-8	2849.59	2.27	51.69	23.33	5.30	1.33	0.84	2.16	5.64	0.87	0.41	0.15
ZDY2	ZY2-TY-11	2850.78	1.67	44.18	18.93	12.44	2.02	2.20	1.73	4.82	0.67	1.60	0.44
ZDY2	ZY2-TY-24	2861.54	2.5	55.37	19.50	7.01	1.11	0.29	1.32	4.65	0.92	0.27	0.09
ZDY2	ZY2-TY-33	2868.8	2.27	55.90	19.29	5.93	1.24	0.74	1.73	5.85	0.80	0.27	0.06
ZDY2	ZY2-TY-37	2870.02	1.68	56.71	20.92	4.40	1.19	0.87	2.21	6.34	0.77	0.23	0.05
ZDY2	ZY2-TY-46	2878.45	2.47	51.58	18.54	10.52	0.65	0.57	1.35	3.40	0.78	0.46	0.06
ZDY2	ZY2-TY-48	2880.01	3.52	54.55	20.78	5.13	1.09	0.85	1.27	3.81	0.78	0.37	0.14
ZDY2	ZY2-TY-52	2882.25	7.43	37.97	15.29	5.78	1.63	11.64	1.21	3.20	0.55	0.18	0.15
ZDY2	ZY2-TY-61	2886.59	1.79	55.41	20.29	6.05	1.26	0.99	1.21	4.10	0.87	0.23	0.14
ZDY2	ZY2-TY-69	2894.67	3.48	61.33	20.48	1.93	0.61	0.21	1.29	3.32	0.78	0.09	0.01
ZDY2	ZY2-TY-75	2897.14	1.32	52.65	15.78	6.36	2.37	4.73	1.64	2.89	0.60	0.32	0.21
ZDY2	ZY2-TY-80	2900.52	1.31	66.51	14.34	3.60	0.73	1.06	1.35	4.14	0.55	0.55	0.04
ZDY2	ZY2-TY-87	2902.32	1.42	61.98	17.12	3.07	1.13	1.74	1.67	4.82	0.58	0.27	0.05
ZDY2	ZY2-TY-92	2905.69	1.25	55.92	17.08	8.61	0.66	1.32	2.18	4.65	0.57	0.23	0.05
ZDY2	ZY2-TY-98	2910.56	2.24	33.80	4.16	2.62	0.68	28.96	0.43	1.33	0.15	0.23	0.01
ZXY1	JX9	3267.87	0.36	60.61	23.01	4.02	0.91	0.22	2.67	6.77	1.03	0.18	0.92
ZXY1	JX13	3274.1	0.8	58.38	27.81	0.80	0.38	0.22	4.07	6.17	1.32	0.09	0.37
ZXY1	JX19	3288.17	0.9	57.61	21.84	5.59	1.18	0.46	0.94	9.56	0.97	0.37	1.19
ZXY1	JX39	3318.5	3.27	58.34	23.77	3.09	0.66	0.15	2.51	8.65	0.83	0.09	0.67
ZXY1	JX41	3321.08	1.57	53.83	16.36	13.20	1.46	0.90	1.16	5.93	0.53	0.46	1.47
ZXY1	JX44	3324.8	2.44	50.83	23.35	9.22	0.93	0.21	2.94	6.84	0.83	0.14	0.94
ZXY1	JX51	3340.75	3.88	53.91	22.50	6.62	0.53	0.83	0.92	4.60	0.97	0.37	0.54

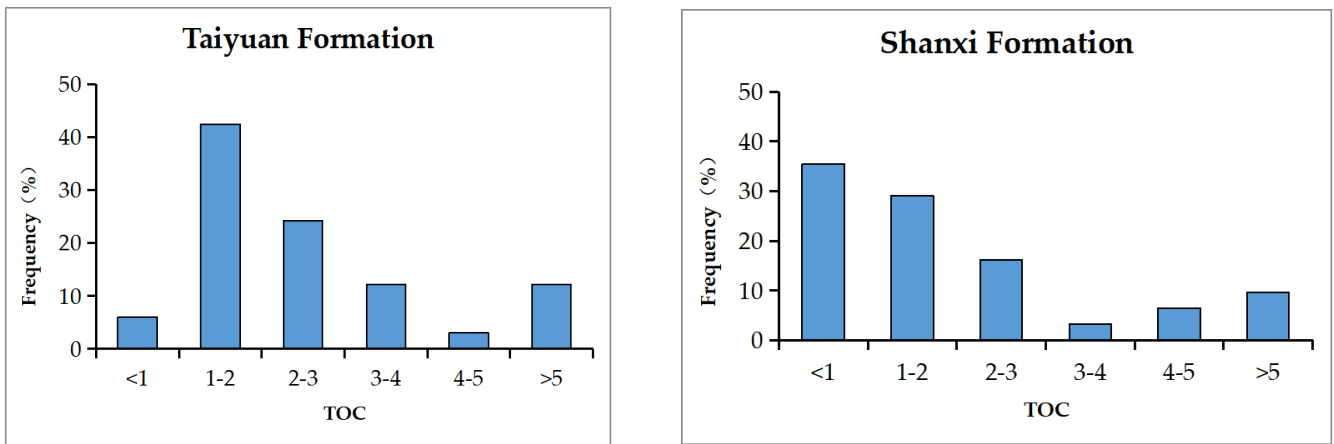


Figure 3. TOC—frequency distribution histogram of the TYF and SXF.

4.2. Major Elements

The primary ME oxides of the TYF and SXF shale samples were SiO₂, Al₂O₃, TFe₂O₃, K₂O, CaO, MgO, MnO, Na₂O, TiO₂, and P₂O₅. The main ME oxides of the TYF were SiO₂, Al₂O₃, TFe₂O₃, K₂O, and CaO, and their contents ranged from 0.34 to 66.51 wt.% (average of 48.1 wt.%), from 0.19 to 28.61 wt.% (average of 19.27 wt.%), from 0.01 to 12.44 wt.% (average of 4.78 wt.%), from 0.02 to 6.84 wt.% (average of 4.45 wt.%), from 0.1 to 28.96 wt.% (average of 2.63 wt.%), respectively. The main ME oxides of the SXF were SiO₂, Al₂O₃, K₂O, and TFe₂O₃, and their contents ranged from 0.58 to 60.61 wt.% (average of 47.23 wt.%), from 0.55 to 33.71 wt.% (average of 23.12 wt.%), from 0.02 to 11.18 wt.% (average of 5.74 wt.%), and from 0.01 to 22.52 wt.% (average of 3.96 wt.%), respectively (Table 1). In general, the TYF and SXF are rich in SiO₂ and comprise siliceous mudstone and argillaceous and siliceous shales (Figure 4).

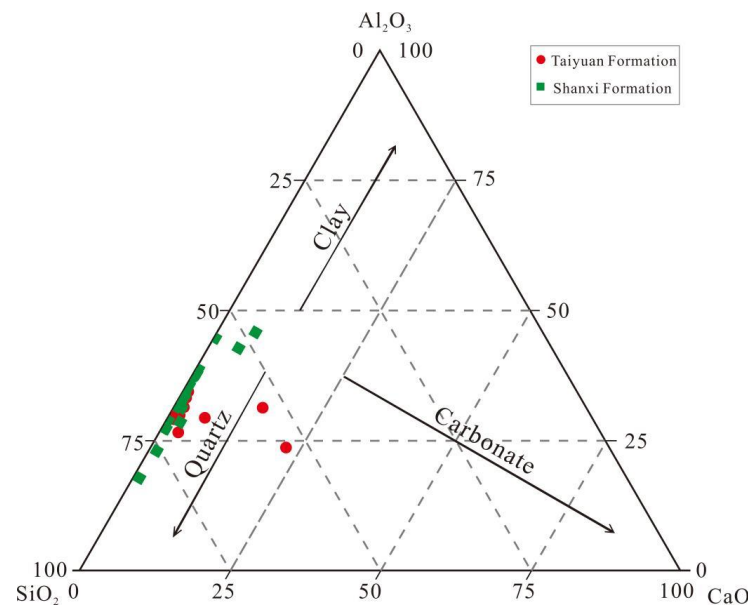


Figure 4. SiO₂–Al₂O₃–CaO ternary diagram for the TYF and SXF shale samples from the MY1 well.

4.3. Trace Elements

The enrichment factor (EF) values can be used to establish the degree of TE enrichment [16]. The equation for EF is as follows:

$$EF = X/Y \tag{1}$$

where X is the content of TEs in minerals or rocks, and Y is the content of TEs in the corresponding basic rocks.

For the TYF, TFs with obvious enrichment ($EF > 1$) included Sr ($EF = 0.47\text{--}14.99$, average of 1.58), Cr ($EF = 0.58\text{--}3.63$, average of 1.14), and TEs with deficit ($EF < 1$) were V, Co, Ni, Ba, Cu, and Zn (Table 2). For the SXF, Ni, Co and Cr showed obvious enrichment ($EF > 1$), which included $EF(Ni) = 0.23\text{--}18.35$, with an average of 2.21, $EF(Co) = 0.35\text{--}3.04$, with an average of 1.86, and $EF(Cr) = 0.08\text{--}3.04$, with an average of 1.07 (Table 2). The TES showing deficits ($EF < 1$) were V, Sr, Cu, and Zn. As shown in Figure 5, compared with the SXF, the shale samples from the TYF show higher EF values in most TEs, except for Co, Ni, and Ba, and the TYF is obviously enriched with Cr and Sr.

Table 2. TE contents of the TYF and SXF in the SNCB.

Well	Sample	Depth (m)	TOC (wt.%)	TEs (ppm)								
				V	Cr	Co	Ni	Sr	Ti	Ba	Cu	Zn
MY1	JX2	2804.81	4.19		15			113	69			38
MY1	JX3	2807.74	1					159	61		70	55
MY1	JX4	2810.32	0.76		137			157	48			154
MY1	JX6	2815.3	0.55		169			517	17			175
MY1	JX7	2819.27	0.53		143			152	65	447		
MY1	JX8	2821.74	1.23		214			222	62	986		46
MY1	JX10	2827.13	1.09		155			274	56		55	
MY1	JX11	2830.72	0.52		156			213	57	482		
MY1	JX12	2831.66	0.44					234	62	694		63
MY1	JX14	2838.32	0.89			114		258	52	813		129
MY1	JX15	2840.23	0.48	246				219	58	652	52	
MY1	JX16	2841.88	2.37					219	54			107
MY1	JX17	2844.32	2.39		175		77	184	51			71
MY1	JX18	2847.16	0.62					217	45	577		
MY1	JX19	2848.82	1.98		138		58	349	42			56
MY1	JX20	2849.51	54.45				41	123	2			27
MY1	JX21	2855.01	66.55			27	41	59	1			
MY1	JX22	2852.36	2.21	129	193		55	134	55			
MY1	JX24	2857.02	4.24				81	203	49	1090		105
MY1	JX31	2884.3	5.1		169		81	212	53	708		111
MY1	JX32	2886.27	1.97	187			77	256	53	791		125
MY1	JX33	2889.34	2.56				138	251	44	1220		94
MY1	JX34	2894.31	1.78				70	279	43	948		113
MY1	JX36	2913.2	3.74		133		69	218	46	506		61
MY1	JX37	2917.42	0.92	327			57	251	50	510		106
MY1	JX39	2923	1.87		417		94	240	45	434	54	83
MY1	JX40	2925.92	1.93				94	240	45	434	54	83
MY1	JX42	2931.5	1.75				60	331	33	473		56
MY1	JX43	2933.86	4.14				85	295	46			189
MY1	JX44	2935.4	61.29		166		58	280	67			
MY1	JX45	2939.27	1.69				58	230	53			68
MY1	JX46	2941.28	2.25		135			264	55			69
MY1	JX47	2943.35	0.66					53	1			
MY1	JX49	2948.32	58.95				67	274	30			82
MY1	JX50	2950.09	5.06					256	40			84
MY1	JX51	2953.09	1.67		147		78	323	43			84
MY1	JX52	2955.71	1.88					459	42	495		53
MY1	JX53	2958.16	2.55	194	156			429	40			90
MY1	JX54	2960.13	1.89		191		111	984	35			137
ZDY2	ZY2-SX-2	2841.67	2.58	125	77.86	17.5	30.2	197.9	56	675	18	88.4
ZDY2	ZY2-TY-8	2849.59	2.27	212	90.22	19.4	60.8	198.9	52	712	31.2	
ZDY2	ZY2-TY-11	2850.78	1.67	219	85.56	19	80.9	301.9	40	773	27.4	162.2
ZDY2	ZY2-TY-24	2861.54	2.5	117	79.58	15.6	28.8	163.9	55	381	23.1	91
ZDY2	ZY2-TY-33	2868.8	2.27	106	72.8	21.3	37.2	190.9	48	514	25.8	86.6

Table 2. Cont.

Well	Sample	Depth (m)	TOC (wt.%)	TEs (ppm)								
				V	Cr	Co	Ni	Sr	Ti	Ba	Cu	Zn
ZDY2	ZY2-TY-37	2870.02	1.68	123	78.54	10.7	24.8	193.9	46	582	23.9	90.4
ZDY2	ZY2-TY-46	2878.45	2.47	137	66.24	28	47.3	251.9	47	318	30.3	50
ZDY2	ZY2-TY-48	2880.01	3.52	155	85.78	12.6	25.2	264.9	47	326	22.3	97.5
ZDY2	ZY2-TY-52	2882.25	7.43	117	60.84	16.2	42.6	439.9	33	680	24.2	123.4
ZDY2	ZY2-TY-61	2886.59	1.79	108	87.4	11.2	23.4	210.9	52	336	24	125.5
ZDY2	ZY2-TY-69	2894.67	3.48	92	64.06	3.6	8.6	227.9	47	308	16.1	96.1
ZDY2	ZY2-TY-75	2897.14	1.32	71	52.1	15.3	16.5	340.9	36	352	17.7	60.6
ZDY2	ZY2-TY-80	2900.52	1.31	94	74.18	16.8	22.8	360.9	33	415	13.3	99.8
ZDY2	ZY2-TY-87	2902.32	1.42	114	80.73	9.2	23.2	379.9	35	516	12	44
ZDY2	ZY2-TY-92	2905.69	1.25	125	79.81	18.2	43.7	367.9	34	566	27	90.3
ZDY2	ZY2-TY-98	2910.56	2.24	51	80.61	4.4	61.8	727.9	9	137	18.4	93.9
ZXY1	JX9	3267.87	0.36	145.6	83.58	19.07	41.8	246	62	769.8	33.1	97.98
ZXY1	JX13	3274.1	0.8	162.3	95.7	11.12	26.16	309	79	890.2	9.37	11.54
ZXY1	JX19	3288.17	0.9	142.4	80.71	13.44	24.77	185.69	58	908	29.1	102.72
ZXY1	JX39	3318.5	3.27	198.1	98.38	36.7	69.22	250.6	50	1355.8	15.02	68.96
ZXY1	JX41	3321.08	1.57	159.8	68.58	109.62	180.66	211	32	905.8	20.6	103.92
ZXY1	JX44	3324.8	2.44	192.6	89.34	31.92	100.52	292	50	1376.2	21.48	44.78
ZXY1	JX51	3340.75	3.88	194.1	88.68	15.33	48.08	268.6	58	534.8	25.3	36.28

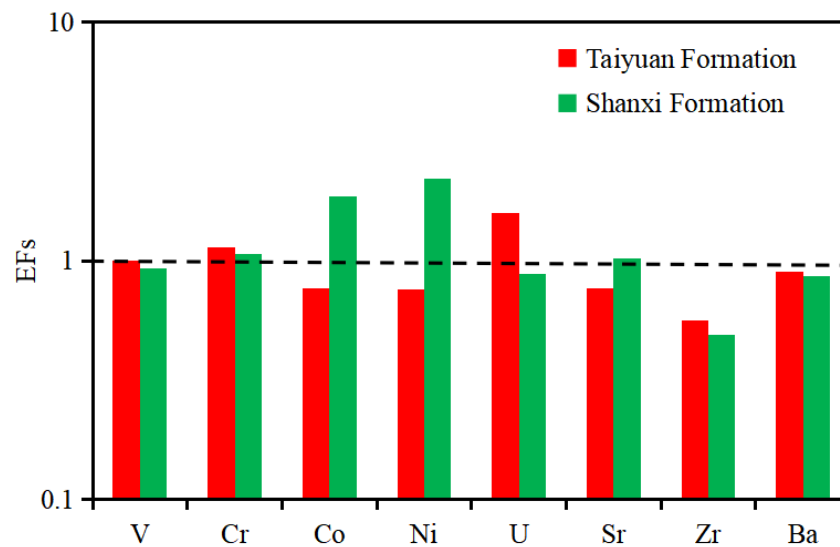


Figure 5. EF diagram of selected TEs for the TYF and SXF shales. The horizontal line (EF = 1) separates the enrichment (above the line) or depletion (below the line) of an element.

4.4. Rare-Earth Elements

REEs and their related parameters for the TYF and SXF in the study area are listed in Table 3. Total rare-earth concentration of the shale in the TYF (Σ REE) ranged from 90.31 to 381.436 ppm, with an average of 224.36 ppm; the range of Σ REE in the SXF was 206.12–376.104 ppm, with an average of 304.21 ppm (Table 3). The average REE concentrations of the shale samples from the TYF and SXF were higher than those of the North American shale composite (NASC, 173.21 ppm) [36] and the post-Archean average Australian shale (PAAS, 184.77 ppm) [37] (Table 3).

Table 3. REE contents (ppm) of the TYF and SXF in the SNCB.

Well	Sample	La	Ce	Pr	Nd	Sm	Eu	Gd	Tb	Dy	Ho	Er	Tm	Yb	Lu	L/H	∑REE	(La/Yb) _N
ZDY2	ZY2-SX-2	55.52	98.32	12.19	43.34	8.13	1.48	6.90	1.07	5.99	1.16	3.51	0.56	3.60	0.55	13.74	242.32	1.14
ZDY2	ZY2-TY-8	45.96	82.09	10.91	38.61	7.43	1.21	5.41	0.78	5.00	1.04	3.24	0.52	3.40	0.52	13.22	206.12	1.00
ZDY2	ZY2-TY-11	63.48	136.85	16.22	60.50	13.00	2.67	13.50	2.02	10.51	1.79	4.75	0.69	4.39	0.66	12.34	331.03	1.07
ZDY2	ZY2-TY-24	57.20	100.16	13.80	47.72	8.50	1.52	7.71	1.12	6.47	1.23	3.67	0.53	3.52	0.55	13.84	253.70	1.20
ZDY2	ZY2-TY-33	54.44	95.00	12.68	46.84	8.95	1.36	7.37	1.11	6.44	1.32	3.81	0.60	3.87	0.60	12.77	244.39	1.04
ZDY2	ZY2-TY-37	51.72	86.11	12.24	42.46	7.46	1.33	6.37	0.84	5.01	1.01	3.13	0.49	3.11	0.52	14.72	221.80	1.23
ZDY2	ZY2-TY-46	47.16	86.14	10.72	38.72	7.15	1.81	6.42	0.92	4.92	0.95	2.77	0.40	2.72	0.43	15.11	211.23	1.28
ZDY2	ZY2-TY-48	47.00	86.71	10.78	37.40	7.57	1.69	6.26	0.89	5.12	1.02	3.05	0.48	3.21	0.49	13.84	211.67	1.08
ZDY2	ZY2-TY-52	52.68	104.65	11.45	38.39	6.80	1.32	5.83	0.79	4.53	0.87	2.65	0.40	2.68	0.41	17.93	233.45	1.45
ZDY2	ZY2-TY-61	49.92	88.44	10.65	36.52	6.93	1.42	5.90	0.81	4.88	0.97	2.84	0.43	2.81	0.44	15.16	212.96	1.31
ZDY2	ZY2-TY-69	48.72	93.61	9.66	33.55	5.66	1.40	4.95	0.62	3.17	0.58	1.61	0.22	1.38	0.21	25.36	205.34	2.61
ZDY2	ZY2-TY-75	49.32	89.70	10.11	34.10	5.98	1.29	5.25	0.72	4.06	0.76	2.28	0.35	2.33	0.37	18.01	206.62	1.56
ZDY2	ZY2-TY-80	64.56	131.10	14.14	52.14	9.86	1.90	7.42	0.89	4.94	0.93	2.84	0.42	2.77	0.44	21.25	294.35	1.72
ZDY2	ZY2-TY-87	60.24	120.42	13.34	47.30	8.20	1.44	6.30	0.84	4.85	0.99	2.91	0.43	2.85	0.43	19.34	270.54	1.56
ZDY2	ZY2-TY-92	66.00	140.30	14.84	52.25	8.52	1.31	6.64	0.87	5.17	1.01	3.06	0.46	2.96	0.45	20.73	303.84	1.65
ZDY2	ZY2-TY-98	26.16	31.86	5.34	20.68	5.31	0.96	4.65	0.73	3.88	0.72	1.96	0.26	1.65	0.26	10.04	104.42	1.17
ZXY1	JX9	75.76	151.34	15.44	60.22	12.65	3.26	10.47	1.29	7.60	1.48	4.42	0.62	4.17	0.60	16.31	349.33	1.34
ZXY1	JX13	64.50	120.72	11.40	39.36	5.65	1.24	4.42	0.60	4.01	0.87	2.87	0.44	3.12	0.46	19.99	259.65	1.53
ZXY1	JX19	82.50	165.12	16.82	64.28	11.07	1.95	8.10	1.05	6.51	1.32	4.11	0.59	4.03	0.58	19.22	368.03	1.51
ZXY1	JX39	88.84	181.50	17.13	56.54	7.34	0.90	5.62	0.89	6.27	1.30	4.18	0.62	4.35	0.62	19.63	376.10	1.51
ZXY1	JX41	59.34	133.20	13.67	53.46	10.10	1.82	9.26	1.25	7.47	1.46	4.42	0.63	4.33	0.63	13.90	301.05	1.01
ZXY1	JX44	90.62	192.42	18.60	67.62	10.95	1.23	10.72	1.77	11.73	2.33	6.91	0.97	6.40	0.90	12.64	423.17	1.04
ZXY1	JX51	51.80	118.68	11.04	40.98	7.04	1.37	5.79	0.84	5.40	1.12	3.57	0.54	3.76	0.54	15.02	252.46	1.02

As shown in the diagram of the PASS-normalized REE distribution patterns (Figure 6), the two curves show nearly the same trend, which may indicate that the REEs of the shale samples from the TYF and SXF come from similar sources. The REE distribution patterns have the characteristics of a relatively flat LREE (from La to Gd) and HREE (from Tb to Lu). The range of L/H (LREE/HREE) for the TYF shale was 10.04–25.36, with an average of 15.96. The L/H (LREE/HREE) of the SXF shale ranged from 12.34–19.99, with an average of 16.04 (Table 2). Ce anomaly (δCe) and Eu anomaly (δEu) was defined as $\delta Ce = Ce_N / (La_N \times Pr_N)^{1/2}$ and $\delta Eu = Eu_N / (Sm_N \times Gd_N)^{1/2}$, respectively [37]. The range of δCe and δEu for the TYF shale was 0.62–1.15 (average of 0.92) and 0.54–1.26 (average of 0.97), respectively; the δCe and δEu of the SXF shale ranged from 0.85 to 1.08 (average of 0.99) and from 0.66 to 1.34 (average of 0.98), respectively (Table 3), indicating that the Ce and Eu anomalies for the TYF and SXF shale were weakly negative.

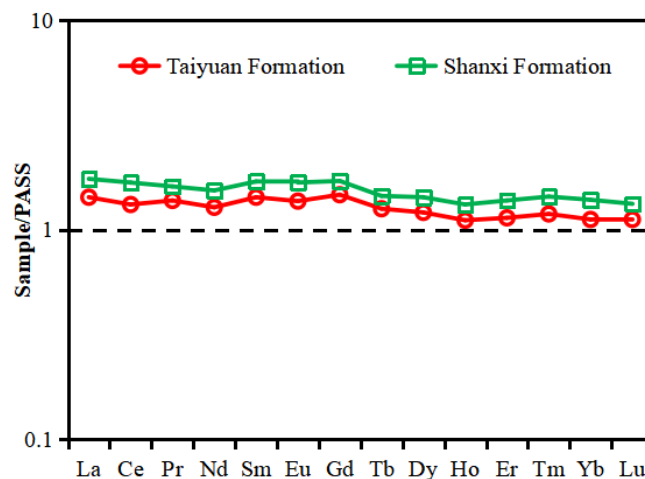


Figure 6. PASS-normalized REE distribution patterns of the TYF and SXF shale samples [37].

5. Discussion

5.1. Paleoclimate

Paleoclimate can affect parent rock weathering, erosion, and sediment transport, and ultimately control the input of terrestrial nutrients and sediment into an ocean [38,39]. The CIA is a typical parameter for reconstructing paleoclimatic conditions [20,21] and for judging the degree of paleoweathering [40,41].

The formula is as follows:

$$CIA = 100 \times Al_2O_3 / (Al_2O_3 + CaO^* + Na_2O + K_2O) \tag{2}$$

The MEs used in the calculations are converted into mole fractions. CaO* is CaO in silicate, that is, the mole fraction of CaO in the whole rock minus the chemically deposited CaO. For CaO* correction, we used

$$CaO^* = CaO - (10/3 \times P_2O_5) \tag{3}$$

After correction, the mole number of CaO* is the minimum value of Na₂O and CaO [42].

Previous studies have shown that the greater the CIA value, the greater the chemical alteration and the climate changes to warmer and wetter conditions. When the CIA value ranges from 50 to 65, the degree of petrochemical weathering is low, indicating a cold and arid climate; when the CIA value ranges from 65 to 85, the degree of petrochemical weathering is medium, indicating a semi-arid and semi-humid climate; and when the CIA value ranges from 85 to 100, the degree of petrochemical weathering is high, indicating a warm and humid climate [20,40]. The CIA range of the TYF shale samples was 74.12–90.02, with an average of 85.58; The CIA range of the SXF shale samples was 80.49–95.03, with an average of 84.88 (Table 4). The paleoclimate and weathering degree of a source rock can be clarified by using the Al₂O₃–(CaO* +Na₂O)–K₂O ternary diagram (Figure 7). Both the TYF and SXF indicate a warm and humid paleoclimate with moderate to strong weathering (Figures 7 and 8).

Table 4. Paleoenvironmental condition analysis.

Environment	Ratios	Geological Units		Index Limit	Reference		
		Taiyuan Formation	Shanxi Formation				
Paleoclimate	CIA	74.12–90.02 (85.58)	80.49–95.03 (84.88)	Cold and arid (50 < CIA < 65)	Semi-arid and semi-humid (65 < CIA < 85)	Warm and humid (85 < CIA < 100)	[20,40,41]
	C-value	0.91–1.08 (1.01)	0.99–1.09 (1.01)	Cold and arid (C-value < 0.4)	Semi-arid and semi-humid (0.4 < C-value < 0.6)	Warm and humid (C-value > 0.6)	[21,22]
Paleo-productivity	P/Ti	0.02–1.83 (0.24)	0.22–0.45 (0.11)				
	B _{bio}	136.98–1376.11 ppm (507.71 ppm)	446.89–1355.71 ppm (828.38 ppm)				
Sedimentary Rate	(La/Yb) _N	0.99–2.6 (1.35)	1.01–1.53 (1.34)				
Paleoredox	Cu/Zn	0.13–0.7 (0.34)	0.2–1.27 (0.48)	Anoxic: Cu/Zn < 0.21	Dysoxic: 0.21 < Cu/Zn < 0.63	Oxic: Cu/Zn > 0.63	[2]
	V/(V + Ni)	0.45–0.91 (0.77)	0.47–1 (0.77)	Anoxic: V/(V + Ni) > 0.6	Dysoxic: 0.46 < V/(V + Ni) < 0.6	Oxic: V/(V + Ni) < 0.46	
Paleosalinity	Sr/Ba	0.21–5.31 (0.78)	0.18–0.44 (0.29)	Fresh water: Sr/Ba < 0.5	Brackish water: 0.5 < Sr/Ba < 1	Saline water: Sr/Ba > 1	[42,43]
	Ca/(Ca + Fe)	0.02–0.98 (0.26)	0.02–0.35 (0.11)	Fresh water: Ca/(Ca + Fe) < 0.4	Brackish water: 0.4 < Ca/(Ca + Fe) < 0.8	Saline water: Ca/(Ca + Fe) > 0.8	

Note: The format of the data is minimum–maximum, and the data in brackets represent the average values.

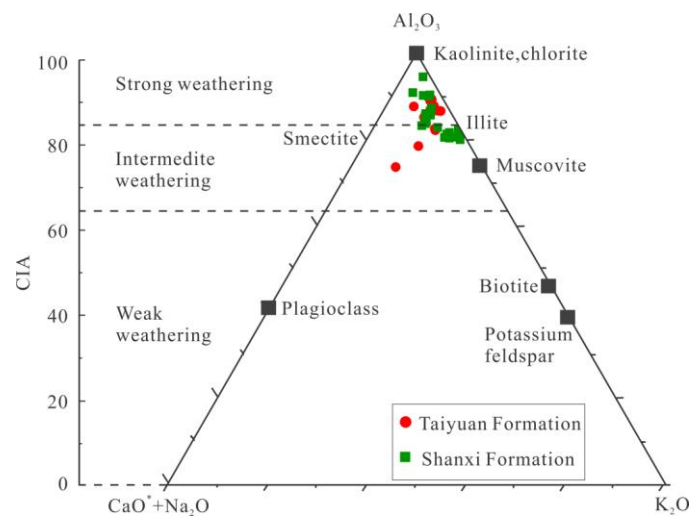


Figure 7. Ternary diagram of molecular proportions $Al_2O_3 - (CaO^* + Na_2O) - K_2O$. The left side shows the CIA scale. The TYF and SXF shale samples display intermediate to strong weathering [20,40].

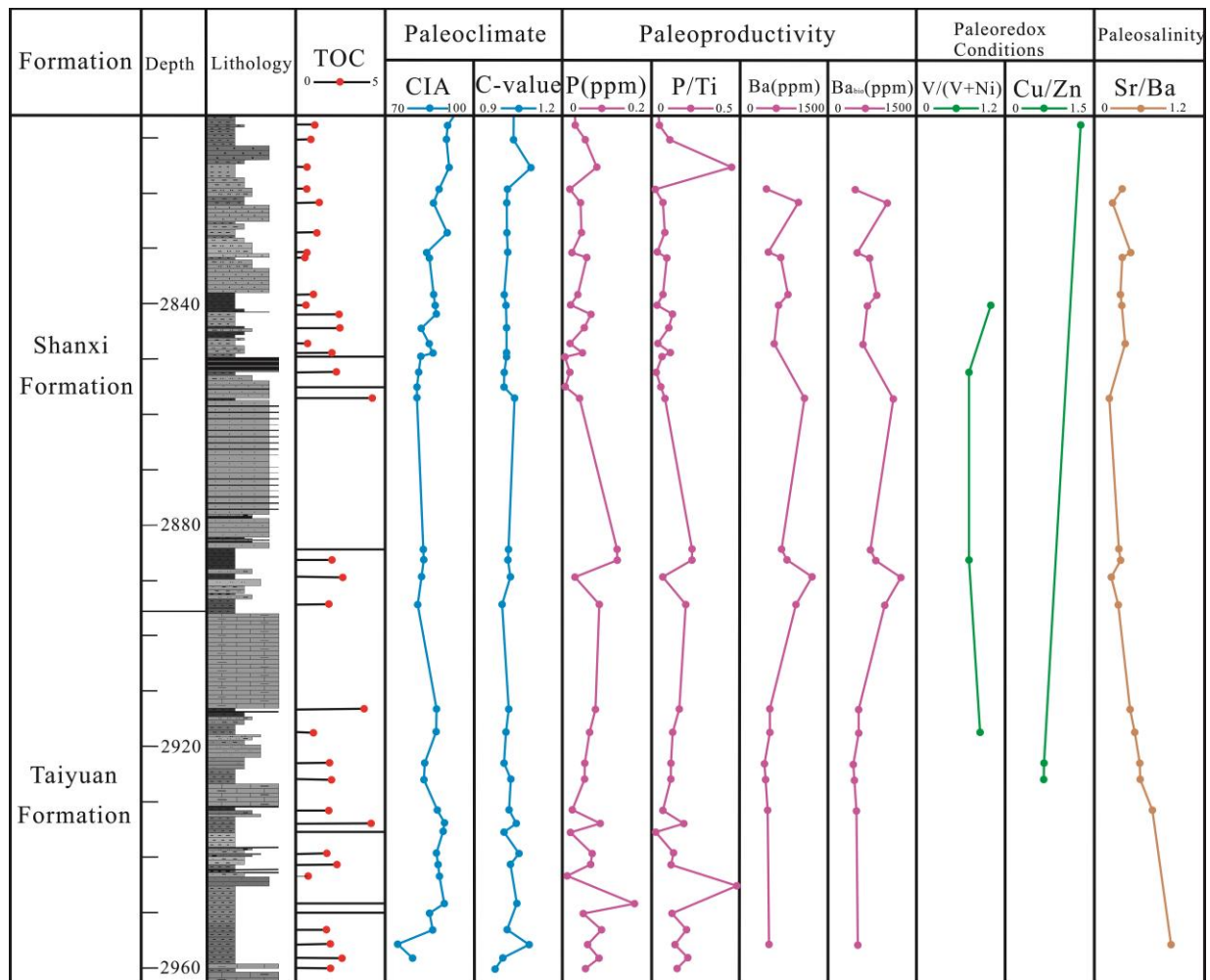


Figure 8. Stratigraphic distributions of TOC, paleoclimate indicators (CIA and C-value), paleoproductivity-related proxies (P, P/Ti, Ba, and Ba_{bio}), paleoredox indexes (V/(V + Ni) and Cu/Zn), and paleosalinity (Sr/Ba and Ca/(Ca + Fe)) in the core of the MY1 well.

The C-value, which is a ratio of transition metals to alkali elements, is also a common proxy for paleoclimate and is defined by the following formula [22]:

$$C\text{-value} = \frac{\Sigma(V + Ni + Mn + Fe + Cr + Co)}{\Sigma(Ca + Mg + Ba + Sr + Na + K)}, \quad (4)$$

When the C-value < 0.4, it indicates a cold and arid climate; when the C-value range is 0.4–0.6, it indicates a semi-humid semi-arid climate; and when the C-value > 0.6, it indicates a warm and humid climate [21,22]. In this study, the C-value of the TYF shale samples ranged from 0.91 to 1.08, with an average of 1.01; the C-value of the SXF shale samples ranged from 0.99 to 1.09, with an average of 1.01 (Table 4). Based on the C-value results, the TYF and SXF were deposited in a warm and humid paleoclimate, which was conducive to the accumulation of OM (Figures 8–10).

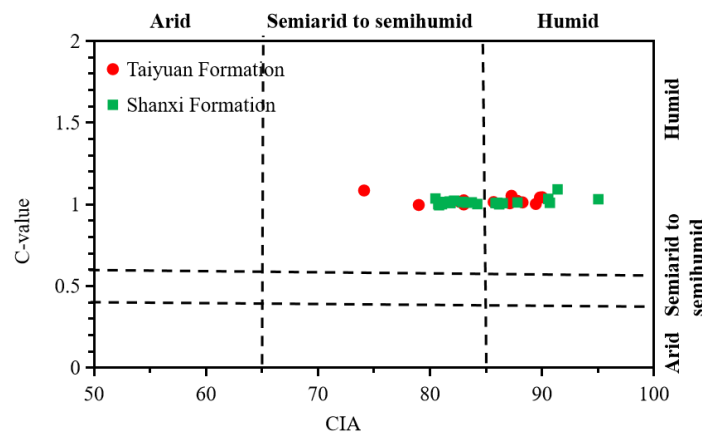


Figure 9. CIA versus C-value of shale from the TYF and SXF.

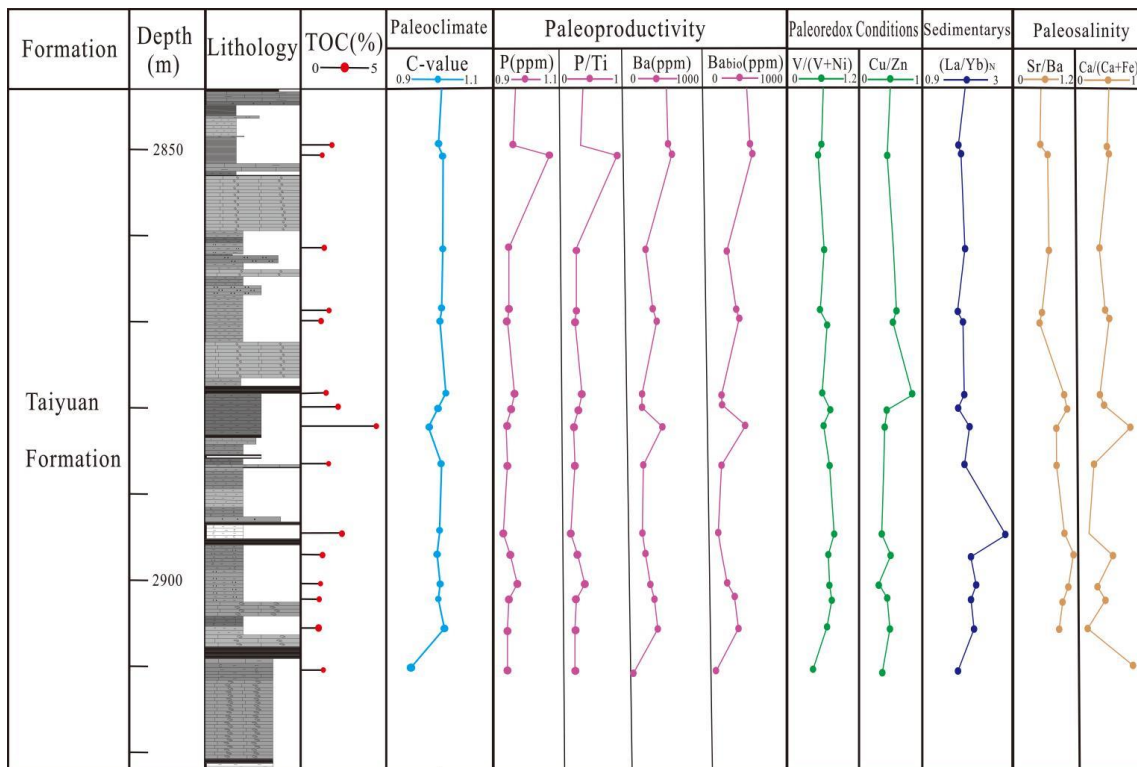


Figure 10. Stratigraphic distributions of TOC, paleoclimate indicators (C-value), paleoproductivity-related proxies (P, P/Ti, Ba, and Ba_{bio}), paleoredox indicators (V/(V + Ni) and Cu/Zn), sedimentation rate ((La/Yb)_N), and paleosalinity indicators (Sr/Ba and Cu/(Cu + Zn)) in the core of the ZDY2 well.

The above paleoclimate indicators (CIA and C-value) collectively indicate that the SNCB experienced a warm and humid paleoclimate during the TYF and SXF deposition period (Figures 7–9). Moreover, there are no obvious differences in the CIAs and C-values for the TYF and SXF shale samples (Figure 8).

5.2. Paleoproductivity

Paleoproductivity, which is affected by water nutrients and biological activities, is a major factor in the accumulation of OM in sediments. Al, Fe, P, Ba, Cu, Zn, Ca, and Mn can be used to estimate the primary productivity [43,44]. However, firm restrictions exist for the selection of elements. P and Ba are commonly used to qualitatively assess biological productivity [2,16,17]. The elements Ba and P provide an effective assessment of the degree of primary productivity [16,17,43]. Ba is preserved as barite, while P is related to algal development [2,17].

Ba is generally combined with SO_4^{2-} and exists in sediments or water bodies in the form of barite (BaSO_4). Barium in sediments can be divided into terrestrial, hydrothermal, and biological sources [45]. However, only the source of Ba (Ba_{bio}) accurately reflects the level of primary productivity. It is necessary to extract abiotic elements from the total elements before evaluating the primary productivity [46,47]. Schroeder et al. [47] proposed Ba_{bio} 's applicable formula as follows:

$$\text{Ba}_{\text{bio}} = \text{Ba}_{\text{total}} - \text{Ba}_{\text{aluminum}} = \text{Ba}_{\text{sample}} - \text{Al}_{\text{sample}} \times (\text{Ba}/\text{Al})_{\text{aluminum}} \quad (5)$$

where $\text{Al}_{\text{sample}}$ and $\text{Ba}_{\text{sample}}$ are the Al and Ba contents of the measured samples, respectively, and $(\text{Ba}/\text{Al})_{\text{aluminum}} = 0.0075$ is a correction factor, which is used to exclude the influence of barium in terrigenous aluminosilicates. Some scholars have also used Ti instead of Al as a correction factor [48].

As shown in Figure 8, the Ba_{bio} content of the TYF shale samples is 136.98–1376.11 ppm, with an average of 507.71 ppm (Table 4), while the Ba_{bio} content of the SXF shale samples is 446.89–1355.71 ppm, with an average of 828.38 ppm (Table 4), indicating that the primary productivity of the SXF is higher than that of the TYF. The value of La/Ce in ancient seawater is 2.8, which is much lower than that in the hydrothermal sediments. The value of La/Ce in hydrothermal sediments is only 0.25; in comparison, the value in normal seawater is usually greater than one. The La/Ce ratio of the shale samples in the TYF is less than 1, ranging from 0.44 to 0.82, with an average value of 0.54; the La/Ce ratio of shale samples in the SXF ranges from 0.45 to 0.56, with an average value of 0.51. This indicates that the shale was affected by strong hot-water sedimentation during the deposition process and is the product of the mixture of hot-water sedimentation and normal seawater sedimentation. Because of the influence of hydrothermal deposition in the study area, it was not appropriate to use Ba_{bio} to judge the paleoproductivity.

The element ratios, P/Ti, Cu/Ti, P/Al, and Cu/Al, are not affected by the supply of terrigenous clastic sediments and can indicate biological productivity [14,49,50]. A higher ratio suggests a higher level of paleoproductivity [51]. The P/Ti of the TYF shale samples ranges from 0.02 to 1.83 (average of 0.24) (Table 4), which is slightly higher than the P/Ti value of PAAS (0.12 [37]), indicating that biological productivity is relatively high. The range of P/Ti of the SXF shale samples is 0.02–0.45 (average of 0.11) (Table 4), which is slightly lower than PAAS, indicating that the paleoproductivity level is medium. According to the P/Ti value, the primary productivity of the TYF is higher than that of the SXF (Figures 8 and 11).

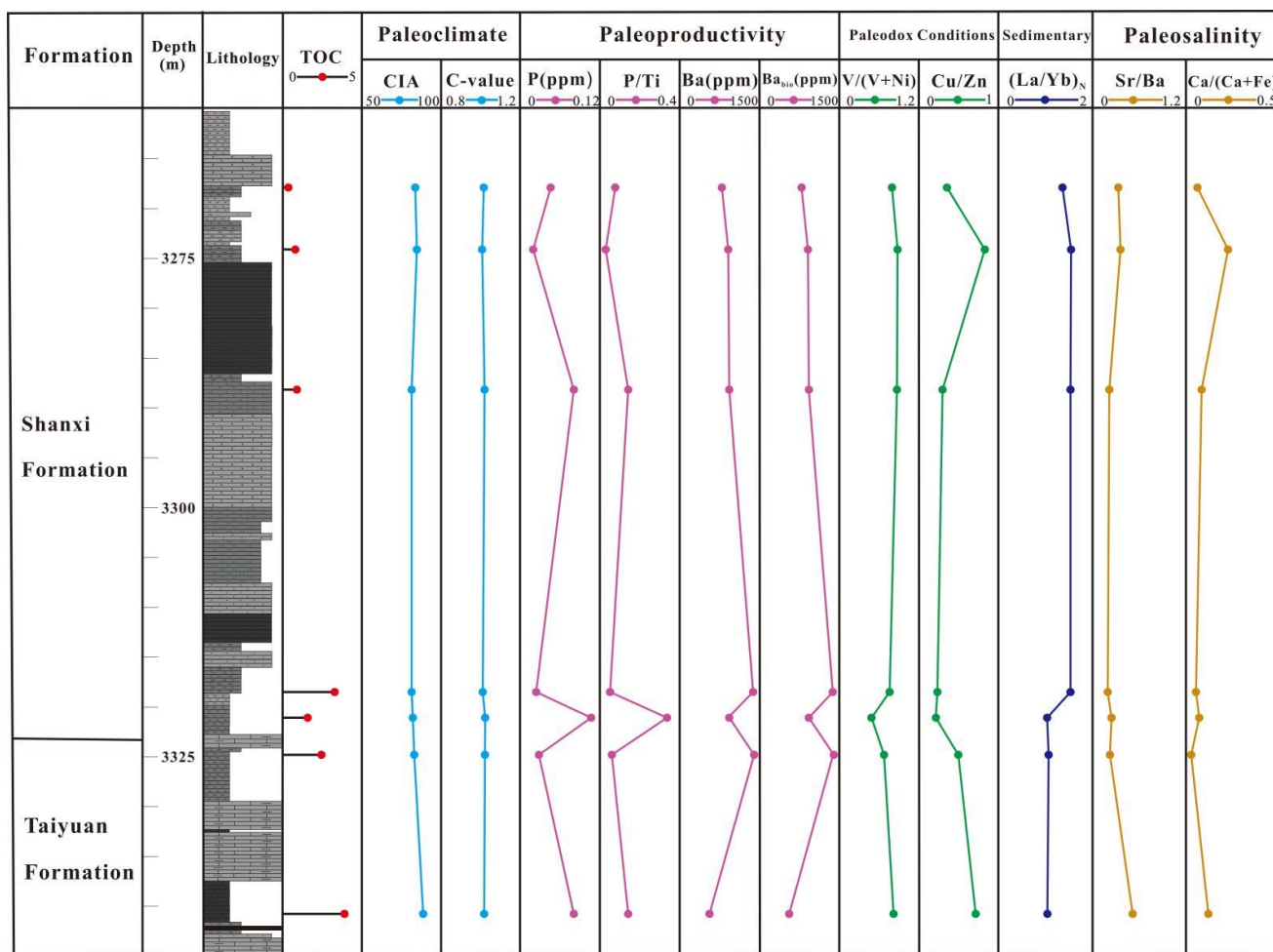


Figure 11. Stratigraphic distributions of TOC, paleoclimate indicators (CIA and C-value), paleoproductivity-related proxies (P, P/Ti, Ba, and B_{bio}), paleoredox indicators (V/(V + Ni) and Cu/Zn), sedimentation rate ((La/Yb)_N), and paleosalinity indicators (Sr/Ba) in the core of the ZXY1 well.

5.3. Sedimentation Rate

OM enrichment is affected by sedimentation rate to some extent [48,52]. A low sedimentation rate and sustained residence time of sediments in a water column would lead to significant differences between LREE and HREE, which can be characterized using the (La/Yb)_N ratio and normalized REE distribution curve [52–55]. The degree of REE fractionation and distribution patterns can be used to establish the sedimentation rate [52,53]. REEs exist in water in combination with debris and suspended solids. Owing to the different residence times in water, the degree of REE fractionation is different [54,55]. When the sedimentation rate is low, REEs have sufficient time to be adsorbed by clay minerals, resulting in a high degree of fractionation, and when the sedimentation rate is high, the situation is the opposite, meaning the sedimentation rate can be deduced from the degree of REE fractionation. Since (La/Yb)_N is a reliable indicator of the degree of REE fractionation, when the value of (La/Yb)_N is close to one, it indicates a high sedimentation rate and a low degree of REE fractionation, and when the (La/Yb)_N value is greater than or less than one, it indicates a low sedimentation rate and a high degree of REE fractionation [56,57]. Besides that, a weak differentiation would lead to a flat REE distribution curve in sediments [54]. As shown in Figure 6, the REE distribution curve trends of the TYF and SXF are relatively gentle, indicating that the shale sedimentation rate was relatively stable during the deposition of the TYF and SXF. The (La/Yb)_N value range of the TYF is 0.99–2.6, with an average of 1.27, while the (La/Yb)_N value of the SXF ranges from 1.01 to 1.53, with

an average of 1.33, showing a relatively high sedimentation rate (Table 4). Because the sedimentation rate of the TYF is closer to one, its sedimentation rate is higher than that of the SXF (Figures 10 and 11). The high sedimentation rate of the TYF shortens the contact time between OM and bacteria, which is conducive to the preservation of OM in oxic water.

5.4. Paleoredox Conditions

TEs, such as the metallic elements U, Th, V, Cr, Ni, Cu, and Zn, are sensitive to the redox environment of water bodies because their solubility is controlled by the redox state of water bodies [19]. U, V, Cr, Ni, Cu, Zn, and other elements are easily soluble in water when the water body provides an oxidizing environment, but they are not soluble in water under reducing conditions [2]. When the water body is an oxygen-poor environment, it is enriched in sediments and almost does not migrate. This provides an indication of ancient water environment and can be used to judge the oxidation–reduction environment of its water body [2,19]. In this study, $V/(V + Ni)$ and Cu/Zn were used to determine the redox conditions of the sedimentary environment.

When the value of $V/(V + Ni)$ is greater than 0.6, it indicates an anoxic environment; when the value of $V/(V + Ni)$ is between 0.46 and 0.6, it indicates a dysoxic sedimentary environment; and when the $V/(V + Ni)$ value is less than 0.46, it indicates an oxygen deposition environment [58,59]. When the Cu/Zn value is less than 0.21, it indicates an anoxic environment; when Cu/Zn ranges from 0.21 to 0.63, it indicates a dysoxic environment; and when the value is greater than 0.63, it indicates an oxic sedimentary environment [2,60]. The $V/(V + Ni)$ value of the TYF samples was between 0.45 and 0.91, with an average of 0.77, while the $V/(V + Ni)$ value of the SXF samples was between 0.47 and 1, with an average of 0.76 (Table 4), indicating that the paleosedimentary environment of both the TYF and SXF was dysoxic–anoxic (Figures 10–12). The Cu/Zn value of the TYF samples ranged from 0.13 to 0.7, with an average of 0.34, while the Cu/Zn value of SXF samples was between 0.2 and 1.27, with an average of 0.48 (Table 4), indicating a dysoxic–anoxic environment (Figures 10–12). The values of $V/(V + Ni)$ and Cu/Zn show that the SNCB was in a dysoxic–anoxic environment during the TYF and SXF periods (Figure 12), while the reducibility of the sedimentary environment of the TYF was slightly greater than that of the SXF.

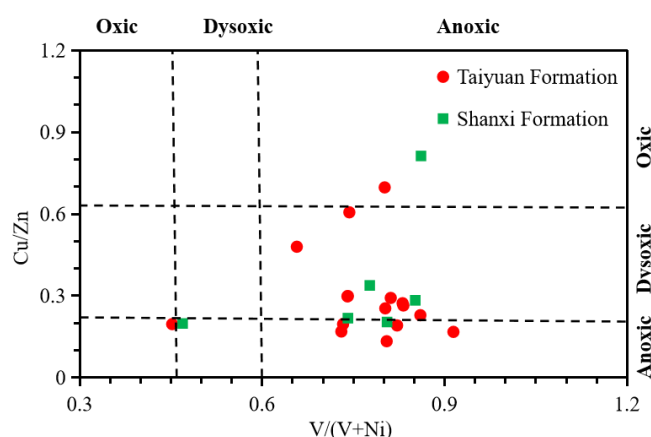


Figure 12. A diagram of $V/(V + Ni)$ versus Cu/Zn of the shale samples from the TYF and SXF.

5.5. Paleosalinity

The Sr/Ba ratio is an important index for judging the salinity of ancient water. Sr is more soluble in water than Ba, meaning Sr migrates further into water, and the Sr/Ba ratio can indirectly reflect continental and marine sediments [60–64]. A Sr/Ba value less than 0.5 indicates a freshwater environment; a value of 0.5–1.0 indicates a brackish water environment; and a value greater than 1.0 suggests a saline water environment [43]. The Sr/Ba value of the TYF samples ranged from 0.21 to 5.31, with an average of 0.78 (Table 4), indicating a freshwater–brackish water environment; the Sr/Ba value of the SXF

samples ranged from 0.18 to 0.44, with an average of 0.29 (Table 4), indicating a freshwater environment, implying that the TYF belonged to marine-continental transitional facies while the SXF was continental (Figures 8, 10 and 13).

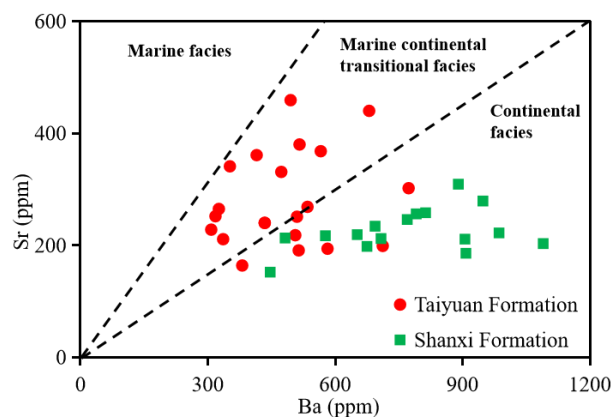


Figure 13. A diagram of Sr/Ba of the shale samples from the TYF and SXF [43].

Moreover, $\text{Ca}/(\text{Ca} + \text{Fe})$ can be used to reflect the salinity level of a water body [11,65]. Generally, the $\text{Ca}/(\text{Ca} + \text{Fe})$ ratio in a seawater environment is greater than 0.8, the ratio in a marine-continental transitional environment is 0.4–0.8, and the ratio in a continental freshwater environment is less than 0.4 [66]. The $\text{Ca}/(\text{Ca} + \text{Fe})$ value of the TYF ranged from 0.02 to 0.98, with an average of 0.26, indicating that the sedimentary environment was freshwater–brackish water, while the $\text{Ca}/(\text{Ca} + \text{Fe})$ value of the SXF ranged from 0.02 to 0.35, with an average of 0.11, indicating that the sedimentary environment was fresh water (Table 4, Figures 8 and 10). The change in the paleosalinity indices (Sr/Ba and $\text{Ca}/(\text{Ca} + \text{Fe})$) both show that the paleosalinity of the TYF is higher than that of the SXF, and that OM is more easily preserved in saline water environments with higher salinity.

5.6. Controlling Factors and Formation Mechanisms of OM Accumulation

OM enrichment is usually affected by many factors, such as primary productivity, redox, paleosalinity, and sedimentation rate, which are complex physical and chemical processes [9,16,18,65]. According to the paleosedimentary environmental indicators, the paleoclimate conditions of the TYF and SXF in the SNCB were similar, both of which were deposited in a warm and humid environment, with relatively high biological productivity and sedimentation rates. Furthermore, the paleosalinity of the TYF and SXF was low during the deposition period, with the environment dominated by a dysoxic–anoxic set of circumstances belonging to marine-continental transitional and continental facies.

From the cross diagram of TOC and the above geochemical indexes (Figure 14), it can be observed that for the TYF and SXF, TOC has a clear correlation with paleoproductivity (P/Ti) (Figure 14a), sedimentation rate ($(\text{La}/\text{Yb})_{\text{N}}$) (Figure 14b), and redox index (Cu/Zn) (Figure 14c), and a weak correlation with paleosalinity (Sr/Ba) (Figure 14d) and paleoclimate (C-value and CIA) (Figure 14e,f), indicating that the main controlling factors of the enrichment of OM in the TYF and SXF are paleoproductivity, sedimentation rate, and redox conditions, while paleoclimate and paleosalinity have relatively little impact on OM accumulation. The correlation between the TOC content of the TYF and these three indicators was better than that of the SXF, indicating that the OM concentration of the TYF was higher (Figure 14).

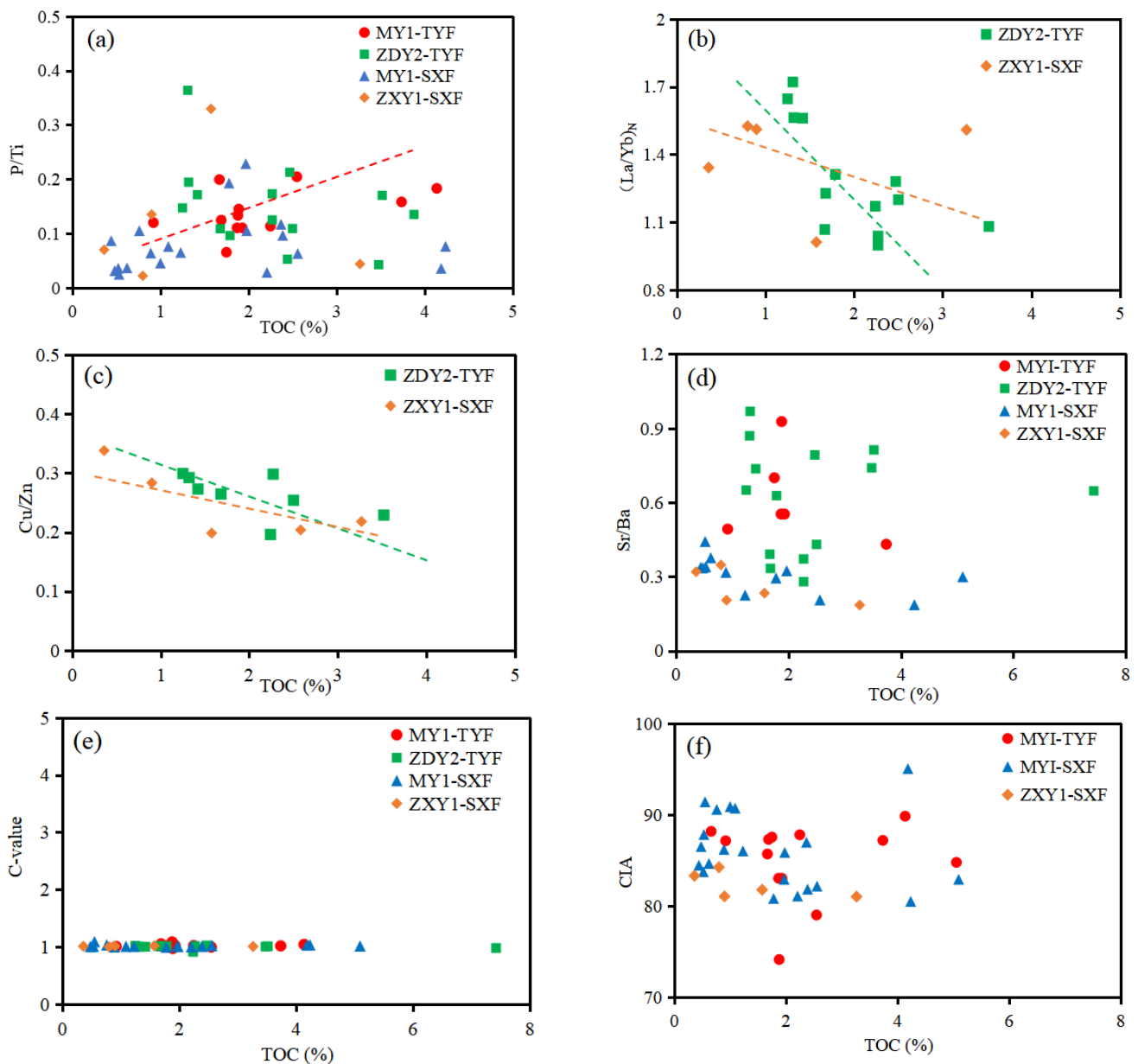


Figure 14. Correlations between TOC contents and productivity index (P/Ti), sedimentation rate index $(La/Yb)_N$, redox index (Cu/Zn), paleosalinity (Sr/Ba), and paleoclimate (C-value, CIA): (a) TOC vs. P/Ti; (b) TOC vs. $(La/Yb)_N$; (c) TOC vs. Cu/Zn; (d) TOC vs. Sr/Ba; (e) TOC vs. C-value; and (f) TOC vs. CIA.

Using the study of the paleoclimate, paleoproductivity, sedimentation rate, redox, and paleosalinity of the TYF and SXF, an OM enrichment model of the Permian TYF and SXF in the SNCB was developed (Figure 15). Two large-scale transgressions occurred in the early and late stages of TYF sedimentation, while the middle stage was the regression stage [67]. Overall, the TYF sea level decreased. The frequent transgression and regression events led to low-energy hydrodynamic conditions, enhanced the reduction of the water body, increased the salinity, reduced the decomposition of OM, and saved more OM. At the same time, the relatively high deposition rate shortened the residence time of aerobic bacteria in OM, reducing the decomposition of OM (Figure 15). Moreover, a high biological productivity increased respiratory oxygen consumption in the water column, leading to OM accumulation. However, during the deposition of the SXF, the seawater retreated from the SNCB and the lithofacies transitioned from marine to continental. The increase in

terrestrial input led to a gradual decrease in salinity; the sedimentary environment changed from an anoxic environment to a poor-oxygen environment, and there was a decrease in paleoproductivity and sedimentation rate, which were not conducive to the deposition and preservation of OM and also reduced TOC. Both the TYF and SXF were deposited in a warm and humid paleoclimate, which was conducive to the growth and proliferation of plants and provided favorable conditions for the later formation of coal seams (Figure 15). In summary, the OM-rich shale of the TYF and SXF in the SNCB is not determined by a single factor but is due to the interaction of many factors, such as paleoproductivity, sedimentation rate, and redox, all of which directly or indirectly affect OM enrichment.

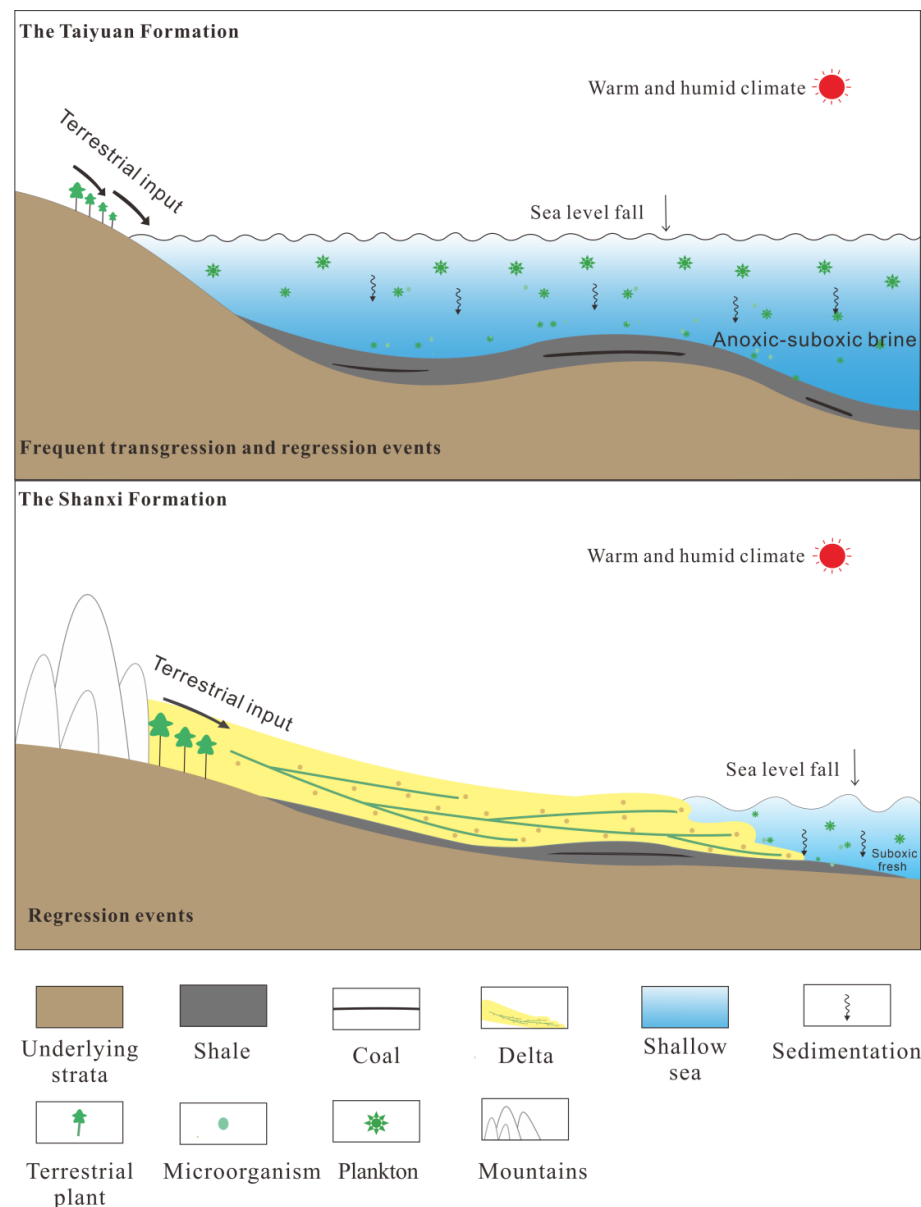


Figure 15. Organic matter enrichment model of the TYF and SXF in the SNCB.

6. Conclusions

1. The TYF and SXF were both deposited in warm and humid environments, with relatively high productivity and sedimentation rates. Moreover, the TYF and SXF were mainly characterized by dysoxic–anoxic environments, belonging to marine–continental transitional and continental facies.

2. The TYF shale mainly developed in a dysoxic–anoxic water environment, with a relatively high sedimentation rate, which reduced the oxidation of OM, caused OM to settle rapidly, and was conducive to OM accumulation. In addition, the high biological productivity increased respiratory oxygen consumption in the water column, leading to OM accumulation. However, the regression event of the SXF reduced the paleoproductivity and sedimentation rate, resulting in a decrease in OM.

3. An OM enrichment model of the TYF and SXF is established. This study is conducive to understanding shale enrichment mechanisms and guiding shale gas exploration in the region. The study could also have broader, global implications for its contributions to the general understanding of shales formed in marine–continental transitional environments.

Author Contributions: Literature search: Y.W. and X.C.; Figure: Y.W. and K.F.; Study design: Y.W., Z.H. and L.W.; Data collection: X.C., K.F. and Z.H.; Data analysis: Y.W.; Data interpretation: Y.W.; Writing: Y.W.; Supervision: X.C. and K.F.; Writing—Review & Editing: Z.H. and L.W. All authors have read and agreed to the published version of the manuscript.

Funding: The National Natural Science Foundation of China (41702152), Special Grant of China Postdoctoral Science Foundation (2018T110124), Foundation of State Key Laboratory of Petroleum Resources and Prospecting, China University of Petroleum, Beijing (PRP/open-1808), and Research on Exploration and Demonstration of Shale Gas in Henan Province (151100311000).

Institutional Review Board Statement: Not applicable.

Informed Consent Statement: Not applicable.

Data Availability Statement: Data supporting the results can be found in the manuscript text, tables, and figures.

Acknowledgments: This work was co-supported by the National Natural Science Foundation of China (41702152), the Special Grant of China Postdoctoral Science Foundation (2018T110124), the Foundation of State Key Laboratory of Petroleum Resources and Prospecting, the China University of Petroleum, Beijing (PRP/open-1808), and the Research on Exploration and Demonstration of Shale Gas in Henan Province (151100311000).

Conflicts of Interest: The authors declare that they have no conflict of interest.

References

- Zhang, S.; Wang, X.; Wang, H.; Bjerrum, C.J.; Hammarlund, E.U.; Costa, M.M.; Connelly, J.N.; Zhang, B.; Su, J.; Canfield, D.E. Sufficient oxygen for animal respiration 1,400 million years ago. *Proc. Natl. Acad. Sci. USA* **2016**, *113*, 1731–1736. [[CrossRef](#)] [[PubMed](#)]
- Tribovillard, N.; Algeo, T.J.; Lyons, T.; Riboulleau, A. Trace metals as paleoredox and paleoproductivity proxies: An update. *Chem. Geol.* **2006**, *232*, 12–32. [[CrossRef](#)]
- Burton, Z.F.M.; Moldowan, J.M.; Magoon, L.B.; Sykes, R.; Graham, S.A. Interpretation of source rock depositional environment and age from seep oil, east coast of New Zealand. *Int. J. Earth Sci.* **2019**, *108*, 1079–1091. [[CrossRef](#)]
- Peters, K.E.; Cassa, M. Chapter 5: Applied source rock geochemistry. In *The Petroleum System—From Source to Trap*; Magoon, L.B., Dow, W.G., Eds.; American Association of Petroleum Geologists Memoir 60: Tulsa, OK, USA, 1994; Volume 14, pp. 93–120.
- Jarvie, D.M.; Hill, R.J.; Ruble, T.E.; Pollastro, R.M. Unconventional shale-gas systems: The Mississippian Barnett Shale of north-central Texas as one model for thermogenic shale-gas assessment. *AAPG Bull.* **2007**, *91*, 475–499. [[CrossRef](#)]
- Johnson, J.E.; Phillips, S.C.; Torres, M.E.; Pinero, E.; Rose, K.K.; Giosan, L. Influence of total organic carbon deposition on the inventory of gas hydrate in the Indian continental margins. *Mar. Pet. Geol.* **2014**, *58*, 406–424. [[CrossRef](#)]
- Burton, Z.F.M. Sediment organic contents required for gas hydrate formation: A survey of published basin and hydrocarbon system models. *Fuels* **2022**, *3*, 280–287. [[CrossRef](#)]
- Zou, C.; Zhu, R.; Chen, Z.Q.; Ogg, J.G.; Wu, S.; Dong, D.; Qiu, Z.; Wang, Y.; Wang, L.; Lin, S.; et al. Organic-matter-rich shales of China. *Earth Sci. Rev.* **2019**, *189*, 51–78. [[CrossRef](#)]
- Lash, G.G.; Blood, D.R. Organic matter accumulation, redox, and diagenetic history of the Marcellus Formation, southwestern Pennsylvania, Appalachian basin. *Mar. Pet. Geol.* **2014**, *57*, 244–263. [[CrossRef](#)]
- Liu, W.; Yao, J.; Tong, J.; Qiao, Y.; Chen, Y. Organic matter accumulation on the Dalong Formation (Upper Permian) in western Hubei, South China: Constraints from multiple geochemical proxies and pyrite morphology. *Palaeogeogr. Palaeoclimatol. Palaeoecol.* **2019**, *514*, 677–689. [[CrossRef](#)]

11. He, J.; Ding, W.; Jiang, Z.; Jiu, K.; Li, A.; Sun, Y. Mineralogical and chemical distribution of the Es3L oil shale in the Jiyang Depression, Bohai Bay Basin (E China): Implications for paleoenvironmental reconstruction and organic matter accumulation. *Mar. Pet. Geol.* **2017**, *81*, 196–219. [[CrossRef](#)]
12. Harris, N.B.; Freeman, K.H.; Pancost, R.D.; White, T.S.; Mitchell, G.D. The character and origin of lacustrine source rocks in the Lower Cretaceous synrift section, Congo Basin, west Africa. *AAPG Bull.* **2004**, *88*, 1163–1184. [[CrossRef](#)]
13. Wu, J.; Liang, C.; Hu, Z.; Yang, R.; Xie, J.; Wang, R.; Zhao, J. Sedimentation mechanisms and enrichment of organic matter in the Ordovician Wufeng Formation–Silurian Longmaxi Formation in the Sichuan Basin. *Mar. Pet. Geol.* **2019**, *101*, 556–565. [[CrossRef](#)]
14. Zeng, S.; Wang, J.; Fu, X.; Chen, W.; Feng, X.; Wang, D.; Song, C.; Wang, Z. Geochemical characteristics, redox conditions, and organic matter accumulation of marine oil shale from the Changliang Mountain area, northern Tibet, China. *Mar. Pet. Geol.* **2015**, *64*, 203–221. [[CrossRef](#)]
15. Moldowan, J.M.; Sundararaman, P.; Schoell, M. Sensitivity of biomarker properties to depositional environment and/or source input in the Lower Toarcian of SW-Germany. *Org. Geochem.* **1986**, *10*, 915–926. [[CrossRef](#)]
16. Ding, J.H.; Zhang, J.C.; Huo, Z.P.; Shen, B.; Shi, G.; Yang, Z.; Li, X.; Li, C. Controlling Factors and Formation Models of Organic Matter Accumulation for the Upper Permian Dalong Formation Black Shale in the Lower Yangtze Region, South China: Constraints from Geochemical Evidence. *ACS Omega* **2021**, *6*, 3681–3692. [[CrossRef](#)]
17. Schmitz, B.; Charisi, S.D.; Thompson, E.I.; Speijer, R.P. Barium, SiO₂ (excess), and P₂O₅ as proxies of biological productivity in the Middle East during the Palaeocene and the latest Palaeocene benthic extinction event. *Terra Nova* **1997**, *9*, 95–99. [[CrossRef](#)]
18. Abart, F.R.; Wagreich, M.; Gier, S.; Ahmed, M.S.; Sami, M. Late Campanian Climatic-Continental Weathering Assessment and Its Influence on Source Rocks Deposition in Southern Tethys, Egypt. *Minerals* **2023**, *13*, 160.
19. Francois, R.A. Study on the regulation of the concentrations of some trace metals (Rb, Sr, Zn, Pb, Cu, V, Cr, Ni, Mn and Mo) in Saanich Inlet Sediments, British Columbia, Canada. *Mar. Geol.* **1988**, *83*, 285–308. [[CrossRef](#)]
20. Nesbitt, H.; Young, G.M. Early Proterozoic climates and plate motions inferred from major element chemistry of lutites. *Nature* **1982**, *299*, 715–717. [[CrossRef](#)]
21. Zhang, B.; Cheng, W.; Zhang, Q.; Li, Y.; Sun, P.; Fathy, D. Occurrence Patterns and Enrichment Influencing Factors of Trace Elements in Paleogene Coal in the Fushun Basin, China. *ACS Earth Space Chem.* **2022**, *6*, 3031–3042. [[CrossRef](#)]
22. Qiu, X.; Liu, C.; Mao, G.; Deng, Y.; Wang, F.; Wang, J. Major, trace and platinum-group element geochemistry of the Upper Triassic nonmarine hot shales in the Ordos basin, Central China. *Appl. Geochem.* **2015**, *52*, 42–52. [[CrossRef](#)]
23. Harris, N.B. *The Deposition of Organic-Carbon-Rich Sediments: Models, Mechanisms, and Consequences*; SEPM Society for Sedimentary Geology: Tulsa, OK, USA, 2005.
24. Murphy, A.E.; Sageman, B.; Hollander, D.J.; Lyons, T.W.; Brett, C.E. Black shale deposition and faunal overturn in the Devonian Appalachian Basin: Clastic starvation, seasonal water-column mixing, and efficient biolimiting nutrient recycling. *Paleoceanography* **2000**, *15*, 280–291. [[CrossRef](#)]
25. Teng, J.; Liu, Y. Analysis of distribution, storage potential and prospect for shale oil and gas in China. *Prog. Geophys.* **2013**, *28*, 1083–1108.
26. Dang, W.; Zhang, J.; Tang, X.; Chen, Q.; Han, S.; Li, Z.; Du, X.; Wei, X.; Zhang, M.; Liu, J.; et al. Shale gas potential of Lower Permian marine-continental transitional black shales in the Southern North China Basin, central China: Characterization of organic geochemistry. *J. Nat. Gas Sci. Eng.* **2016**, *28*, 639–650. [[CrossRef](#)]
27. Liang, Q.; Zhang, X.K.; Tian, J.; Sun, X.; Chang, H. Geological and geochemical characteristics of marine-continental transitional shale from the Lower Permian Taiyuan Formation, Taikang Uplift, southern North China Basin. *Mar. Pet. Geol.* **2018**, *98*, 229–242. [[CrossRef](#)]
28. Peng, Y. *The Shale Gas Accumulation Conditions of Taiyuan Formation in Southern North China Basin*; China University of Geosciences: Beijing, China, 2020.
29. Huo, Z.P.; Zhang, J.C.; Li, P.; Tang, X.; Yang, X.; Qiu, Q.; Dong, Z.; Li, Z. An improved evaluation method for the brittleness index of shale and its application—A case study from the southern north China basin. *J. Nat. Gas Sci. Eng.* **2018**, *59*, 47–55. [[CrossRef](#)]
30. Xu, H.L.; Zhao, Z.J.; Lu, F.L.; Yang, Y.; Tang, Z.; Sun, G.; Xu, Y. Tectonic evolution of the Nanhuabei area and analysis about its petroleum potential. *Geotect Metallog.* **2004**, *28*, 450–463.
31. Yu, H.; Lv, F.; Guo, Q.; Lu, W.; Wu, J.; Han, S. Proto-sediment basin types and tectonic evolution in the southern edge of North China Pla. *Earth-Sci. Rev.* **2005**, *27*, 111–117.
32. Zhou, X.; Ni, C.; Yang, F. The Paleozoic prototype basins and their tectonic deformation in North China and their controlling effects upon hydrocarbon accumulation. *Pet. Nat. Gas Geol.* **2010**, *31*, 779–794.
33. Diao, Y.; Wei, J.; Li, Z.; Cao, H.; Li, X. Late carboniferous-early permian sequence stratigraphy and paleogeography in the southern North China Basin. *Acta Geol. Sin.* **2011**, *35*, 88–94.
34. Zhang, M.Q. *Controlling Factor for Shale Enrichment of the Permian Shale in Southern North China Basin*; China University of Geosciences: Beijing, China, 2016.
35. Huo, Z.P.; Gao, J.; Zhang, J.C.; Zhang, D.; Liang, Y. Role of overlying and underlying limestones in the natural hydraulic fracturing of shale sections: The case of marine-continental transitional facies in the Southern North China Basin. *Energy Rep.* **2021**, *7*, 8711–8729. [[CrossRef](#)]
36. Haskin, L.A.; Wildeman, T.R.; Haskin, M.A. An accurate procedure for the determination of the rare earths by neutron activation. *J. Radioanal. Chem.* **1968**, *1*, 337–348. [[CrossRef](#)]

37. Taylor, S.R.; McLennan, S.M. *The Continental Crust: Its Composition and Evolution*; Blackwell Scientific Publications: Oxford, UK, 1985; pp. 117–140.
38. Bonis, N.R.; Ruhl, M.; Kürschner, W. Climate change driven black shale deposition during the end-Triassic in the western Tethys. *Palaeogeogr. Palaeoclimatol. Palaeoecol.* **2010**, *290*, 151–159. [[CrossRef](#)]
39. Burton, Z.F.M.; McHargue, T.; Kremer, C.H.; Bloch, R.B.; Gooley, J.T.; Jaikla, C.; Harrington, J. Peak Cenozoic warmth enabled deep-sea sand deposition. *Sci. Rep.* **2023**, *13*, 1276. [[CrossRef](#)] [[PubMed](#)]
40. Fedo, C.M.; Nesbitt, H.W.; Young, G.M. Unraveling the effects of potassium metasomatism in sedimentary rocks and paleosols, with implications for paleoweathering conditions and provenance. *Geology* **1995**, *23*, 921–924. [[CrossRef](#)]
41. Price, J.R.; Velbel, M.A. Chemical weathering indices applied to weathering profiles developed on heterogeneous felsic metamorphic parent rocks. *Chem. Geol.* **2003**, *202*, 397–416. [[CrossRef](#)]
42. McLennan, S.M.; Hemming, S.R.; McDaniel, D.K.; Hanson, G.N. Geochemical approaches to sedimentation, provenance, and tectonics. *Spec. Pap. Geol. Soc. Am.* **1993**, *284*, 21–40.
43. Chen, H.; Tang, D.; Chen, S.; Tang, S. Geochemical characteristics of mudstones from the lower cretaceous strata of the Jixi Basin, NE China: Implications for organic matter enrichment. *Int. J. Coal Geol.* **2021**, *249*, 103904. [[CrossRef](#)]
44. Brumsack, H.J. The trace metal content of recent organic carbon-rich sediments; implications for Cretaceous black shale formation. *Palaeogeogr. Palaeoclimatol. Palaeoecol.* **2006**, *232*, 344–361. [[CrossRef](#)]
45. Dymond, J.; Suess, E.; Lyle, M. Barium in Deep-Sea Sediment: A Geochemical Proxy for Paleoproductivity. *Paleoceanography* **1992**, *7*, 163–181. [[CrossRef](#)]
46. Shen, J.; Schoepfer, S.D.; Feng, Q.; Zhou, L.; Yu, J.; Song, H.; Wei, H.; Algeo, T.J. Marine productivity changes during the end-Permian crisis and Early Triassic recovery. *Earth Sci. Rev.* **2015**, *149*, 136–162. [[CrossRef](#)]
47. Schroeder, J.; Murray, R.W.; Leinen, M.S.; Pflaum, R.; Janecek, T.R. Barium in equatorial Pacific carbonate sediment: Terrigenous, oxide, and biogenic associations. *Paleoceanography* **1997**, *12*, 125–146. [[CrossRef](#)]
48. Ibach, L.E.J. Relationship between sedimentation rate and total organic carbon content in ancient marine sediments. *AAPG Bull.* **1982**, *66*, 170–188.
49. Algeo, T.J.; Maynard, J.B. Trace-element behavior and redox facies in core shales of Upper Pennsylvanian Kansas-type cyclothems. *Chem. Geol.* **2004**, *206*, 289–318. [[CrossRef](#)]
50. Wu, Z.; Zhao, X.; Wang, E.; Pu, X.; Lash, G.; Han, W.; Zhang, W.; Feng, Y. Sedimentary environment and organic enrichment mechanisms of lacustrine shale: A case study of the Paleogene Shahejie Formation, Qikou Sag, Bohai Bay Basin. *Palaeogeogr. Palaeoclimatol. Palaeoecol.* **2021**, *573*, 110404. [[CrossRef](#)]
51. Pan, Y.; Huang, Z.; Li, T.; Guo, X.; Xu, X.; Chen, X. Environmental response to volcanic activity and its effect on organic matter enrichment in the Permian Lucaogou Formation of the Malang Sag, Santanghu Basin, Northwest China. *Palaeogeogr. Palaeoclimatol. Palaeoecol.* **2020**, *560*, 110024. [[CrossRef](#)]
52. Tyson, R.V. Sedimentation rate, dilution, preservation and total organic carbon: Some results of a modelling study. *Org. Geochem.* **2001**, *32*, 333–339. [[CrossRef](#)]
53. Sageman, B.B.; Murphy, A.E.; Werne, J.P.; Ver Straeten, C.A.; Hollander, D.J.; Lyons, T.W. A tale of shales: The relative roles of production, decomposition, and dilution in the accumulation of organic-rich strata, Middle–Upper Devonian, Appalachian basin. *Chem. Geol.* **2003**, *195*, 229–273. [[CrossRef](#)]
54. Ruhlin, D.E.; Owen, R.M. The rare earth element geochemistry of hydrothermal sediments from the East Pacific Rise: Examination of a seawater scavenging mechanism. *Geochim. Cosmochim. Acta* **1986**, *50*, 393–400. [[CrossRef](#)]
55. Murray, R.W.; Brink, M.B.T.; Gerlach, D.C.; Russ, G.P.; Jones, D. Rare earth, major, and trace elements in chert from the Franciscan Complex and Monterey Group, California: Assessing REE sources to fine-grained marine sediments. *Geochim. Cosmochim. Acta* **1991**, *55*, 1875–1895. [[CrossRef](#)]
56. Tenger, Liu, W.; Xu, Y.; Chen, J. Comprehensive geochemical identification of highly evolved marine carbonate rocks as hydrocarbon-source rocks as exemplified by the Ordos Basin. *Sci. China Ser. D* **2006**, *49*, 384–396. [[CrossRef](#)]
57. Doner, Z.; Kumral, M.; Demirel, I.H.; Hu, Q. Geochemical characteristics of the Silurian shales from the central Taurides, southern Turkey: Organic matter accumulation, preservation and depositional environment modeling. *Mar. Pet. Geol.* **2019**, *102*, 155–175. [[CrossRef](#)]
58. Hatch, J.R.; Leventhal, J.S. Relationship between inferred redox potential of the depositional environment and geochemistry of the Upper Pennsylvanian (Missourian) Stark Shale Member of the Dennis Limestone, Wabaunsee County, Kansas, U.S.A. *Chem. Geol.* **1992**, *99*, 65–82. [[CrossRef](#)]
59. Li, W.; Li, X.; Ding, Q.; Chen, S.; Zhang, J. Geochemical characteristics and paleoenvironment of Cretaceous Jiufotang Formation in Xiushui Basin, northern Liaoning. *Glob. Geol.* **2019**, *38*, 154–161.
60. Mei, S. Application of rock chemistry in the study of Presinian sedimentary environment and the source of Uranium mineralization in Hunan Province. *Land Resour. Her.* **1988**, *7*, 25–31.
61. Ye, L.; Qi, T.; Peng, H. Depositional environment analysis of Shanxi formation in Eastern Ordos Basin. *Acta Sedimentol. Sin.* **2008**, *26*, 202–210.
62. Fu, J.; Deng, X.; Wang, Q.; Li, J.; Qiu, J.; Hao, L.; Zhao, Y. Densification and hydrocarbon accumulation of Triassic Yanchang Formation Chang 8 Member, Ordos Basin, NW China: Evidence from geochemistry and fluid inclusions. *Pet. Explor. Dev.* **2017**, *44*, 48–57. [[CrossRef](#)]

63. Xiao, J. Geochemical Indicators of Sedimentary Environments—A Summary. *Earth Environ.* **2011**, *39*, 405–414.
64. Wang, P.W.; Chen, Z.L.; Li, X.J. Geochemical characteristics and environmental significance of Dengying formation of Upper Sinian in Qiannan Depression. *Geoscience* **2011**, *25*, 1059–1065.
65. Liu, C.; Liu, K.; Wang, X.; Wu, L.; Fan, Y. Chemostratigraphy and sedimentary facies analysis of the Permian Lucaogou Formation in the Jimusaer Sag, Junggar Basin, NW China: Implications for tight oil exploration. *J. Asian Earth Sci.* **2019**, *178*, 96–111. [[CrossRef](#)]
66. Guo, L.; Zhang, S.; Xie, X.; Zhong, S.; Huang, C.; Chen, B. Geochemical characteristics and organic matter enrichment of the Dongyuemiao member mudstone of Lower Jurassic in the Western Hubei-Eastern Chongqing. *Sci. J. Earth Sci.* **2017**, *42*, 1235–1246.
67. Shang, B.H.; Ni, Y.; Song, H.; Liu, S.; Zhang, L. Sequence stratigraphic framework of Late Paleozoic coal measures and their sedimentary evolution in Henan, Yprovince. *Coal Geol. Explor.* **2012**, *40*, 1–5.

Disclaimer/Publisher’s Note: The statements, opinions and data contained in all publications are solely those of the individual author(s) and contributor(s) and not of MDPI and/or the editor(s). MDPI and/or the editor(s) disclaim responsibility for any injury to people or property resulting from any ideas, methods, instructions or products referred to in the content.